

Remnant of binary black-hole mergers: New simulations and peak luminosity studies

James Healy and Carlos O. Lousto

*Center for Computational Relativity and Gravitation,
School of Mathematical Sciences, Rochester Institute of Technology,
85 Lomb Memorial Drive, Rochester, New York 14623*

(Dated: November 1, 2016)

We present the results of 61 new simulations of nonprecessing spinning black hole binaries with mass ratios $q = m_1/m_2$ in the range $1 \leq q \leq 1/3$ and individual spins covering the parameter space $-0.85 \leq \alpha_{1,2} \leq 0.85$. We additionally perform 10 new simulations of nonspinning black hole binaries with mass ratios covering the range $1/6 \leq q < 1$. We follow the evolution for typically the last ten orbits before merger down to the formation of the final remnant black hole. This allows for assessment of the accuracy of our previous empirical formulae for relating the binary parameters to the remnant final black hole mass, spin and recoil. We use the new simulation to improve the fit to the above remnant formulae and add a formula for the peak luminosity of gravitational waves, produced around the merger of the two horizons into one. We find excellent agreement (typical errors $\sim 0.1 - 0.2\%$) for the mass and spin, and $\sim 5\%$ for the recoil and peak luminosity. These formulae have direct application to parameter estimation techniques applied to LIGO observations of gravitational waves from binary black hole mergers.

PACS numbers: 04.25.dg, 04.25.Nx, 04.30.Db, 04.70.Bw

I. INTRODUCTION

The breakthroughs [1–3] in numerical relativity allow us to make detailed predictions for the gravitational waves from the latest inspiral, plunge, merger and ring-down of black hole binary systems (BHB). The first generic, long-term precessing binary black hole evolution without any symmetry was performed in Ref. [4], where a detailed comparison with post-Newtonian $\ell = 2, 3$ waveforms was made. Those predictions have been recently confirmed (notably with quite similar parameters to the first detection [5]) by the direct observation of gravitational waves [6–8] from such binary systems and its comparison to theory [9].

Numerical relativity techniques also allow us to explore the late binary dynamics, beyond the post-Newtonian regime. For instance to study the *hangup*, i.e. the role individual black hole spins play to delay or accelerate their merger [10], the determination of the magnitude and direction of the *recoil* velocity of the final merged black hole [11–13], and the *flip-flop* of individual spins during the orbital phase [14–16].

In a hierarchical search or parameter estimation of gravitational wave signals, aligned spin binaries, i.e. non-precessing, play an important role, since the full 7 dimensional (assuming very small eccentricities) parameter space of a binary is currently very hard to cover with solely full numerical waveforms.

In Ref. [17] we used 37 original runs and those available in the literature to determine fitting formulae that related aligned spin binaries initial parameters (q, α_1, α_2) to the final black hole mass, spin and recoil (m_f, α_f, V_f). Here we revisit this scenario and perform 71 new runs that allow us to evaluate the errors of the previous fit-

ting formulae and then use the new results to improve the fittings.

The waveforms produced by the new simulations, covering mass ratios in the range $1/3 \leq q \leq 1$ for the spinning binaries and $1/6 \leq q < 1$ for nonspinning ones will form the basis of the new RIT's waveform catalog and supplement current catalogs [18, 19], all of them can be used as a data bank for search and parameter identification of gravitational wave signals [20].

The paper is organized as follows. Section II describes the methods and criteria for producing the new simulations. Sec. III describe the results obtained for the remnant properties, i.e. final mass, spin, and recoil, and the comparison with the predicted values from the phenomenological formula of Ref. [17]. We also introduce a fitting formula for the gravitational wave's peak luminosity and use the new runs to better fit the mass, spin and recoil parameters. The new fitting parameters are determined and provided in Tables III and IV. In Sec. IV, the use and potential extensions to this work to precessing binaries are discussed. In the appendices we give tables containing the remnant information and fitting parameters, as well as detailed studies of the numerical convergence and error estimates for those quantities.

II. FULL NUMERICAL EVOLUTIONS

We evolve the following BBH data sets using the LAZEV [21] implementation of the moving puncture approach [2, 3] with the conformal function $W = \sqrt{\chi} = \exp(-2\phi)$ suggested by Ref. [22]. For the run presented here, we use centered, sixth-order finite differencing in space [23] and a fourth-order Runge Kutta time integra-

tor (Note that we do not upwind the advection terms.) and a 7th-order Kreiss-Oliger dissipation operator. This sixth-order spatial finite difference allow us to gain a factor $\sim 4/3$ with the respect to the eight-order implementation due to the reduction of the ghost zones from 4 to 3. We also allowed for a Courant factor $CFL = 1/3$ instead of the previous $CFL = 0.25$ [24] gaining another speedup factor of $4/3$. We verified that for this relaxing of the time integration step we still conserve the horizon masses and spins of the individual black holes during evolution and the phase of the gravitational waveforms to acceptable levels. This plus the use of the new Xsede supercomputer *Comet* at SDSC [25] lead to typical evolution speeds of $250M/day$ on 16 nodes. Note that our previous [15, 26] comparable simulations averages $\sim 100M/day$.

Our code uses the EINSTEINTOOLKIT [27, 28] / CACTUS [29] / CARPET [30] infrastructure. The CARPET mesh refinement driver provides a “moving boxes” style of mesh refinement. In this approach, refined grids of fixed size are arranged about the coordinate centers of both holes. The CARPET code then moves these fine grids about the computational domain by following the trajectories of the two BHs.

We use AHFINDERDIRECT [31] to locate apparent horizons. We measure the magnitude of the horizon spin using the *isolated horizon* (IH) algorithm detailed in Ref. [32] and as implemented in Ref. [33]. Note that once we have the horizon spin, we can calculate the horizon mass via the Christodoulou formula $m_H = \sqrt{m_{\text{irr}}^2 + S_H^2/(4m_{\text{irr}}^2)}$, where $m_{\text{irr}} = \sqrt{A/(16\pi)}$, A is the surface area of the horizon, and S_H is the spin angular momentum of the BH (in units of M^2). In the tables below, we use the variation in the measured horizon irreducible mass and spin during the simulation as a measure of the error in computing these quantities. We measure radiated energy, linear momentum, and angular momentum, in terms of the radiative Weyl Scalar ψ_4 , using the formulas provided in Refs. [34, 35]. However, rather than using the full ψ_4 , we decompose it into ℓ and m modes and solve for the radiated linear momentum, dropping terms with $\ell > 6$. The formulas in Refs. [34, 35] are valid at $r = \infty$. We extract the radiated energy-momentum at finite radius and extrapolate to $r = \infty$. We find that the new perturbative extrapolation described in Ref. [36] provides the most accurate waveforms. While the difference of fitting both linear and quadratic extrapolations provides an independent measure of the error.

A. New simulations

In order to supplement our previous work on aligned binaries [17] we consider a set of full numerical simulations with initial configurations as described in Table I and Table II. These simulations cover the parameter space of aligned (and counteraligned) spins for comparable mass ratios q up to 1:3. We have chosen comparable mass ratios and spin magnitude $\alpha_i \leq 0.85$ as they

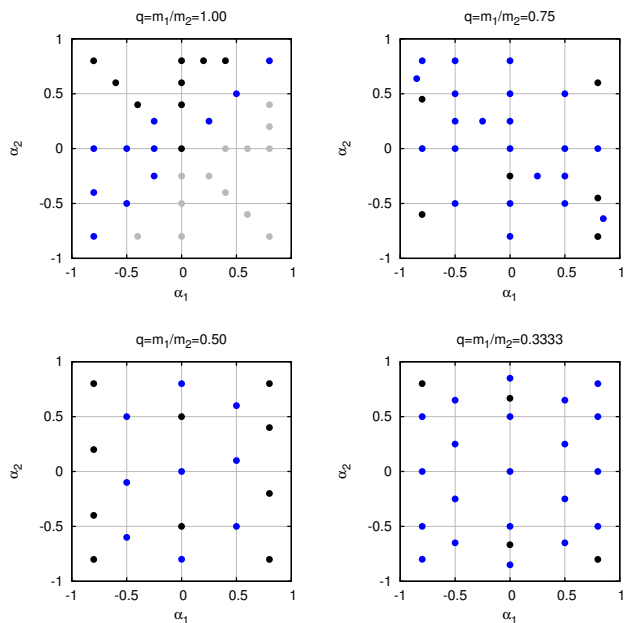


FIG. 1. Initial configuration of the simulated binaries. The black dots represent the previous simulations reported in [17] and those in blue are the new simulations of this paper. Those points in light gray are obtained by the symmetry $1 \leftrightarrow 2$ of the case $q = 1$.

are less demanding computationally than the more extreme cases. In particular, they span over the mass ratios and spins of the parameters estimated for the black hole binaries associated with the gravitational wave signals GW150914 ($q = 0.81$) and GW151226 ($q = 0.52$) and the transient LVT151012 ($q = 0.57$) [8]. We have also considered initial separations of the binary such that they produce at least 6 orbits prior to merger, with typical simulations producing 8-10 orbits and above. The study of higher spins and longer waveforms (either through simulations or hybridization) will be the subject of a forthcoming paper by the authors.

Note that our new runs supplement the previous study as depicted in Fig. 1. Those runs have been in part selected to cover the parameter space of aligned binaries on surfaces of equal $\tilde{S}_0 = (\alpha_2 + q\alpha_1)/(1+q)$ and in part motivated to better model the gravitational wave events mentioned above. They also supplement other independent studies, thus providing a tighter grid of simulations that have been used to directly estimate the parameters of the black hole binary that produced GW150914[20]. One of the runs provided here (with $q = 0.82$) was compared with a totally independent simulation by the SXS collaboration finding excellent agreement for the waveform as well as the final remnant parameters [9].

TABLE I. Initial data parameters for the quasi-circular configurations with a smaller mass black hole (labeled 1), and a larger mass spinning black hole (labeled 2). The punctures are located at $\vec{r}_1 = (x_1, 0, 0)$ and $\vec{r}_2 = (x_2, 0, 0)$, with momenta $P = \pm(P_r, P_t, 0)$, spins $\vec{S}_i = (0, 0, S_i)$, mass parameters m^p/m , horizon (Christodoulou) masses m^H/m , total ADM mass M_{ADM} , and dimensionless spins $a/m_H = S/m_H^2$. The configuration are denoted by QX_Y_Z, where X gives the mass ratio m_1^H/m_2^H , Y gives the spin of the smaller BH (a_1/m_H^2), and Z gives the spin of the larger BH (a_2/m_H^2).

Run	x_1/m	x_2/m	P_r/m	P_t/m	m_1^p/m	m_2^p/m	S_1/m^2	S_2/m^2	m_1^H/m	m_2^H/m	M_{ADM}/m	a_1/m_1^H	a_2/m_2^H
1	-8.81	2.94	-3.69e-04	0.06634	0.2405	0.6585	0	-0.2812	0.25	0.75	0.9934	0	-0.5
2	-7.69	2.56	-4.73e-04	0.06929	0.2393	0.6575	0	0.2812	0.25	0.75	0.9924	0	0.5
3	-9.19	3.06	0	0.06508	0.2408	0.3912	0	-0.4781	0.25	0.75	0.9937	0	-0.85
4	-7.50	2.50	-4.80e-04	0.0691	0.2391	0.3903	0	0.4781	0.25	0.75	0.9921	0	0.85
5	-9.00	3.00	-3.34e-04	0.06503	0.2137	0.7226	-0.03125	-0.1406	0.25	0.75	0.9935	-0.5	-0.25
6	-8.25	2.75	-4.03e-04	0.0674	0.2131	0.7219	-0.03125	0.1406	0.25	0.75	0.9929	-0.5	0.25
7	-8.25	2.75	-4.30e-04	0.0682	0.213	0.7219	0.03125	-0.1406	0.25	0.75	0.993	0.5	-0.25
8	-7.69	2.56	-4.89e-04	0.06974	0.2124	0.7213	0.03125	0.1406	0.25	0.75	0.9924	0.5	0.25
9	-9.38	3.12	0	0.06404	0.214	0.5871	-0.03125	-0.3656	0.25	0.75	0.9938	-0.5	-0.65
10	-7.69	2.56	-4.69e-04	0.06921	0.2125	0.5857	-0.03125	0.3656	0.25	0.75	0.9924	-0.5	0.65
11	-8.62	2.88	-4.02e-04	0.06741	0.2133	0.5866	0.03125	-0.3656	0.25	0.75	0.9934	0.5	-0.65
12	-7.50	2.50	-4.90e-04	0.06938	0.2123	0.5856	0.03125	0.3656	0.25	0.75	0.9922	0.5	0.65
13	-8.81	2.94	0	0.06526	0.1495	0.7415	-0.05	0	0.25	0.75	0.9934	-0.8	0
14	-8.25	2.75	0	0.06687	0.1492	0.7409	0.05	0	0.25	0.75	0.9929	0.8	0
15	-9.38	3.12	0	0.06388	0.1498	0.659	-0.05	-0.2812	0.25	0.75	0.9938	-0.8	-0.5
16	-7.88	2.62	0	0.06869	0.1489	0.6576	-0.05	0.2812	0.25	0.75	0.9926	-0.8	0.5
17	-8.25	2.75	0	0.06841	0.1491	0.658	0.05	-0.2812	0.25	0.75	0.9931	0.8	-0.5
18	-7.50	2.50	0	0.0694	0.1486	0.6573	0.05	0.2812	0.25	0.75	0.9922	0.8	0.5
19	-10.12	3.38	0	0.06125	0.1502	0.462	-0.05	-0.45	0.25	0.75	0.9943	-0.8	-0.8
20	-7.12	2.38	0	0.07049	0.1483	0.4601	0.05	0.45	0.25	0.75	0.9918	0.8	0.8
21	-8.67	4.33	-3.74e-04	0.0738	0.3233	0.4089	0	-0.3556	0.3333	0.6667	0.9929	0	-0.8
22	-7.33	3.67	-4.99e-04	0.07755	0.3217	0.4079	0	0.3556	0.3333	0.6667	0.9914	0	0.8
23	-8.33	4.17	-3.91e-04	0.07451	0.2868	0.6543	-0.05556	-0.04444	0.3333	0.6667	0.9925	-0.5	-0.1
24	-8.00	4.00	-4.07e-04	0.07478	0.2865	0.654	0.05556	0.04444	0.3333	0.6667	0.9921	0.5	0.1
25	-6.67	3.33	-7.42e-04	0.08443	0.2846	0.5813	-0.05556	0.2222	0.3333	0.6667	0.9909	-0.5	0.5
26	-7.33	3.67	0	0.08082	0.2855	0.5823	0.05556	-0.2222	0.3333	0.6667	0.9916	0.5	-0.5
27	-8.67	4.33	-3.74e-04	0.07384	0.2871	0.5449	-0.05556	-0.2667	0.3333	0.6667	0.9929	-0.5	-0.6
28	-7.67	3.83	-4.33e-04	0.07537	0.2861	0.544	0.05556	0.2667	0.3333	0.6667	0.9917	0.5	0.6
29	-5.71	4.29	-9.10e-04	0.09328	0.4146	0.5435	0	0.08163	0.4286	0.5714	0.9899	0	0.25
30	-6.29	4.71	0	0.0895	0.4158	0.4965	0	-0.1633	0.4286	0.5714	0.9908	0	-0.5
31	-6.29	4.71	0	0.08653	0.4159	0.4966	0	0.1633	0.4286	0.5714	0.9905	0	0.5
32	-6.29	4.71	0	0.0904	0.4157	0.3477	0	-0.2612	0.4286	0.5714	0.9909	0	-0.8
33	-6.29	4.71	0	0.08564	0.416	0.3478	0	0.2612	0.4286	0.5714	0.9905	0	0.8
34	-5.71	4.29	-9.31e-04	0.0939	0.404	0.5435	-0.04592	0.08163	0.4286	0.5714	0.9899	-0.25	0.25
35	-5.71	4.29	-9.59e-04	0.09446	0.4039	0.5435	0.04592	-0.08163	0.4286	0.5714	0.99	0.25	-0.25
36	-6.29	4.71	-7.22e-04	0.08936	0.3693	0.559	-0.09184	0	0.4286	0.5714	0.9908	-0.5	0
37	-6.29	4.71	-6.54e-04	0.08722	0.3693	0.5591	0.09184	0	0.4286	0.5714	0.9906	0.5	0
38	-5.71	4.29	0	0.09422	0.3682	0.5435	-0.09184	0.08163	0.4286	0.5714	0.9899	-0.5	0.25
39	-5.71	4.29	-9.34e-04	0.09383	0.3681	0.5436	0.09184	-0.08163	0.4286	0.5714	0.99	0.5	-0.25
40	-6.29	4.71	0	0.09061	0.3692	0.4964	-0.09184	-0.1633	0.4286	0.5714	0.9909	-0.5	-0.5
41	-6.29	4.71	0	0.08753	0.3694	0.4965	-0.09184	0.1633	0.4286	0.5714	0.9906	-0.5	0.5
42	-6.29	4.71	0	0.08839	0.3693	0.4965	0.09184	-0.1633	0.4286	0.5714	0.9907	0.5	-0.5
43	-6.29	4.71	0	0.08553	0.3694	0.4966	0.09184	0.1633	0.4286	0.5714	0.9905	0.5	0.5
44	-6.29	4.71	0	0.0866	0.3694	0.3478	-0.09184	0.2612	0.4286	0.5714	0.9906	-0.5	0.8
45	-6.29	4.71	0	0.0897	0.2586	0.559	-0.1469	0	0.4286	0.5714	0.9909	-0.8	0
46	-6.29	4.71	0	0.08633	0.2586	0.5592	0.1469	0	0.4286	0.5714	0.9906	0.8	0
47	-5.71	4.29	0	0.09286	0.2579	0.3469	-0.1469	0.2612	0.4286	0.5714	0.99	-0.8	0.8
48	-6.29	4.71	0	0.08779	0.2192	0.4479	-0.1561	0.2082	0.4286	0.5714	0.9908	-0.85	0.6375
49	-6.29	4.71	0	0.088	0.2192	0.448	0.1561	-0.2082	0.4286	0.5714	0.9908	0.85	-0.6375
50	-6.73	5.52	-4.90e-04	0.08312	0.4021	0.5136	-0.08932	0.09963	0.4505	0.5495	0.9914	-0.44	0.33
51	-5.50	5.50	0	0.09112	0.4871	0.4327	0	-0.125	0.5	0.5	0.9905	0	-0.5
52	-5.50	5.50	0	0.0919	0.4871	0.303	0	-0.2	0.5	0.5	0.9907	0	-0.8
53	-6.00	6.00	-5.50e-04	0.0856	0.4757	0.4882	-0.0625	0	0.5	0.5	0.9912	-0.25	0
54	-6.00	6.00	-5.66e-04	0.08617	0.4757	0.4757	-0.0625	-0.0625	0.5	0.5	0.9912	-0.25	-0.25
55	-6.00	6.00	-5.34e-04	0.08504	0.4758	0.4757	-0.0625	0.0625	0.5	0.5	0.9911	-0.25	0.25
56	-6.00	6.00	-5.06e-04	0.08392	0.4758	0.4758	0.0625	0.0625	0.5	0.5	0.991	0.25	0.25
57	-5.50	5.50	0	0.09247	0.4326	0.4326	-0.125	-0.125	0.5	0.5	0.9907	-0.5	-0.5
58	-5.50	5.50	-6.38e-04	0.08751	0.4328	0.4328	0.125	0.125	0.5	0.5	0.9903	0.5	0.5
59	-6.50	6.50	0	0.08277	0.3042	0.4556	-0.2	-0.1	0.5	0.5	0.992	-0.8	-0.4
60	-5.50	5.50	0	0.09411	0.3029	0.3029	-0.2	-0.2	0.5	0.5	0.991	-0.8	-0.8
61	-5.00	5.00	-8.19e-04	0.09128	0.3023	0.3023	0.2	0.2	0.5	0.5	0.9895	0.8	0.8

TABLE II. Initial data parameters for the quasi-circular configurations as in Table I but for the non-spinning systems.

Run	x_1/m	x_2/m	P_r/m	P_t/m	m_1^p/m	m_2^p/m	S_1/m^2	S_2/m^2	m_1^H/m	m_2^H/m	M_{ADM}/m	a_1/m_1^H	a_2/m_2^H
62	-9.00	1.50	-2.19e-04	0.0459	0.1358	0.8511	0	0	0.1429	0.8571	0.9952	0	0
63	-8.96	1.79	-2.55e-04	0.05116	0.1589	0.8266	0	0	0.1667	0.8333	0.9947	0	0
64	-8.80	2.20	-3.08e-04	0.05794	0.1913	0.7923	0	0	0.2	0.8	0.994	0	0
65	-8.44	2.81	-3.83e-04	0.06677	0.2401	0.7411	0	0	0.25	0.75	0.993	0	0
66	-8.04	3.21	-4.50e-04	0.07262	0.2751	0.7045	0	0	0.2857	0.7143	0.9924	0	0
67	-7.33	3.67	-5.72e-04	0.0802	0.3216	0.6557	0	0	0.3333	0.6667	0.9916	0	0
68	-7.19	4.31	-5.46e-04	0.08206	0.3632	0.6138	0	0	0.375	0.625	0.9914	0	0
69	-7.05	4.70	-5.29e-04	0.08281	0.3883	0.5887	0	0	0.4	0.6	0.9913	0	0
70	-6.29	4.71	-6.86e-04	0.08828	0.4159	0.5591	0	0	0.4286	0.5714	0.9907	0	0
71	-6.49	5.51	-5.29e-04	0.08448	0.4477	0.529	0	0	0.4595	0.5405	0.9912	0	0

III. REMNANT AND LUMINOSITY FITTING FORMULAE

Besides the interest in producing waveforms for direct comparison with observation, the simulation of orbiting black hole binaries produce information about the final remnant of the merger of the two holes. This was already the subject of studies using the Lazarus approach [37] previous to the breakthrough that allowed longer accurate computations and lead to numerous empirical formulae relating the initial parameters (individual masses and spins) of the binary to those of the final remnant, such as its mass [38], spin [39, 40], and recoil velocity [17, 41–43], or algebraic properties of the final metric [44, 45]. The computation of the peak luminosity has also recently been the subject of interest in relation to the observation of gravitational waves [8], [46].

In general, the mapping of the 7-dimensional space (assuming quasicircular orbits) of a binary into the 4-dimensional space of the final black hole mass and spin is a complicated process because of the task of accurately accounting for the precession of the individual spins particularly during the latest stages. In the case studied here, aligned binaries, the symmetry of the problem prevents orbital plane precession and we have obtained accurate representations of the empirical remnant formulae by a fourth order polynomial expansion in the appropriate binary variables [42, 47] and imposing the particle limit analytically [17].

In order to verify the predictions of these formulae we cover the parameter space of comparable mass binaries with a new set of 71 simulations that nearly doubles the original 37 used in [17] and we extend the fittings to also model the peak Luminosity. We summarize the results of the evolution of the new 61 spinning and 10 nonspinning binaries in tables V–XIII given in the appendix.

Table V for the 61 spinning cases and table VI for the 10 nonspinning ones display the orbital initial frequency of the binary as well as its initial measured eccentricity (small but not zero as we used PN quasicircular orbits [48, 49], but did not seek to iterate the parameters towards zero as in [50]). We also provide the eccentricity at merger (as the binary circularizes by emitting gravitational waves) and number of orbits before the merger actually takes place in the simulation. Finally, for cross reference to other papers using these runs (as for instance in [20]) we provide the technical name used to identify the run.

Because the puncture initial data we use [51] assumes a conformally flat 3-metric it has a non-physical (albeit generally small) wave content that gets radiated away or absorbed by the holes. In order to provide a more physical set of initial parameters to be used into the remnant formulae, we extract the parameters of the black holes after the values of the horizon masses and spin settles. We observe that evaluating those at a time $t = 150M$ after the beginning of the simulation is very accurate and we provide those values in Table VII and Table VIII for

the 61 spinning and 10 nonspinning binaries respectively.

The remnant properties are displayed in Tables IX and X for the final mass and spin of the product of the merger of the 61 spinning and 10 nonspinning binaries. We compare in those tables the determination of the final mass and spin from the direct measure of the isolated horizon quantities using [32] or from the conservation of the ADM mass and momentum of the system, i.e. subtracting from them the radiated energy and momentum carried by the waveforms to obtain the remnant mass and spin of the final black hole. The level of agreement of those quantities provides an estimate of the errors in determining the final mass and spin of the hole. In our experience using the isolated horizon quantities provides an excellent approximation with a much smaller error than the above estimate.

Finally we also provide Tables XI – XIII with the recoil velocity and peak luminosity as directly computed from the waveforms (adding up to $\ell = 6$ modes). We study in appendix B the error estimates of in those quantities produced by the finite difference resolutions we used in the simulations and incorporate this information into the fitting formulae below.

A. Fitting final mass and spin

We compare this new simulations results with the predictions of the previous fit to evaluate the errors of the previous fitting given in Ref. [17].

The fitting formula for M_{rem} is given by,

$$\begin{aligned} \frac{M_{\text{rem}}}{m} = (4\eta)^2 \Big\{ & M_0 + K_1 \tilde{S}_{\parallel} + K_{2a} \tilde{\Delta}_{\parallel} \delta m + K_{2b} \tilde{S}_{\parallel}^2 + \\ & K_{2c} \tilde{\Delta}_{\parallel}^2 + K_{2d} \delta m^2 + K_{3a} \tilde{\Delta}_{\parallel} \tilde{S}_{\parallel} \delta m + \\ & K_{3b} \tilde{S}_{\parallel} \tilde{\Delta}_{\parallel}^2 + K_{3c} \tilde{S}_{\parallel}^3 + \\ & K_{3d} \tilde{S}_{\parallel} \delta m^2 + K_{4a} \tilde{\Delta}_{\parallel} \tilde{S}_{\parallel}^2 \delta m + \\ & K_{4b} \tilde{\Delta}_{\parallel}^3 \delta m + K_{4c} \tilde{\Delta}_{\parallel}^4 + K_{4d} \tilde{S}_{\parallel}^4 + \\ & K_{4e} \tilde{\Delta}_{\parallel}^2 \tilde{S}_{\parallel}^2 + K_{4f} \delta m^4 + K_{4g} \tilde{\Delta}_{\parallel} \delta m^3 + \\ & K_{4h} \tilde{\Delta}_{\parallel}^2 \delta m^2 + K_{4i} \tilde{S}_{\parallel}^2 \delta m^2 \Big\} + \\ & \left[1 + \eta(\tilde{E}_{\text{ISCO}} + 11) \right] \delta m^6, \quad (1) \end{aligned}$$

and the fitting formula for the final spin has the form,

$$\begin{aligned}
\alpha_{\text{rem}} = \frac{S_{\text{rem}}}{M_{\text{rem}}^2} = (4\eta)^2 \Big\{ & L_0 + L_1 \tilde{S}_{\parallel} + \\
& L_{2a} \tilde{\Delta}_{\parallel} \delta m + L_{2b} \tilde{S}_{\parallel}^2 + L_{2c} \tilde{\Delta}_{\parallel}^2 + L_{2d} \delta m^2 + \\
& L_{3a} \tilde{\Delta}_{\parallel} \tilde{S}_{\parallel} \delta m + L_{3b} \tilde{S}_{\parallel} \tilde{\Delta}_{\parallel}^2 + L_{3c} \tilde{S}_{\parallel}^3 + \\
& L_{3d} \tilde{S}_{\parallel} \delta m^2 + L_{4a} \tilde{\Delta}_{\parallel} \tilde{S}_{\parallel}^2 \delta m + L_{4b} \tilde{\Delta}_{\parallel}^3 \delta m + \\
& L_{4c} \tilde{\Delta}_{\parallel}^4 + L_{4d} \tilde{S}_{\parallel}^4 + L_{4e} \tilde{\Delta}_{\parallel}^2 \tilde{S}_{\parallel}^2 + \\
& L_{4f} \delta m^4 + L_{4g} \tilde{\Delta}_{\parallel} \delta m^3 + \\
& L_{4h} \tilde{\Delta}_{\parallel}^2 \delta m^2 + L_{4i} \tilde{S}_{\parallel}^2 \delta m^2 \Big\} + \\
& \tilde{S}_{\parallel} (1 + 8\eta) \delta m^4 + \eta \tilde{J}_{\text{ISCO}} \delta m^6. \quad (2)
\end{aligned}$$

Note that the two formulae above impose the particle limit by including the ISCO dependencies.

The results of the comparison of all available data in Ref. [17] plus the new data and SXS data for the mass and spins (175 runs in total) with the previous formulae are displayed as the red histograms in Fig. 2 and are labeled as V1. We also compare these same data points with the new fitted parameters (See below) and the results are summarized by the blue histograms labeled as V2.

From Fig. 2, we observe that the predictions using the previous formulae for the final mass and spin are very accurate even for the new runs. Note that in general the new runs started at longer separations and used a different numerical evolution system, as mentioned in the previous section. Given this success we will continue to use the form of the fitting formulae as in Ref. [17] but will include now all runs available to improve the statistical errors in the fitting of the 19 parameters in each formula.

We thus provide a full updated set of fitting parameters using all the 71 new runs, an additional set of 68 SXS spin-aligned runs from their BBH catalog [52], and the 36 runs used in Ref. [17] to produce a more accurate set of remnant formulae. The results are summarized in Table III for the final mass and spin.

The results of the new fits can be summarized in Fig. 3 where we observe the values of the fit compared to those computed by the simulations for the final mass and the residuals of the fit in both the differences and percentage of the differences. Notably the residuals are limited to differences in the masses of $\pm 1.2 \times 10^{-3}$, corresponding to percentages of less than 0.13%.

The minimum mass (and hence the maximum radiated energy) as a function of the mass ratio and spins ($M_{\text{rem}}(q, \alpha_1, \alpha_2)$) occurs for equal mass binaries bearing maximum spins along the orbital angular momentum. This corresponds also to the maximum hangup effect [10]. Evaluation of the above fitted formula gives us $M_{\text{rem}}(1, 1, 1) = 0.88672$ which corresponds to radiating above 11% of the initial ADM mass of the binary system. The minimum energy radiated occurs in the particle limit, but we can evaluate the minimum energy radiated for the equal-mass case. In this case, minimum radiation occurs due to the anti-hangup, when both

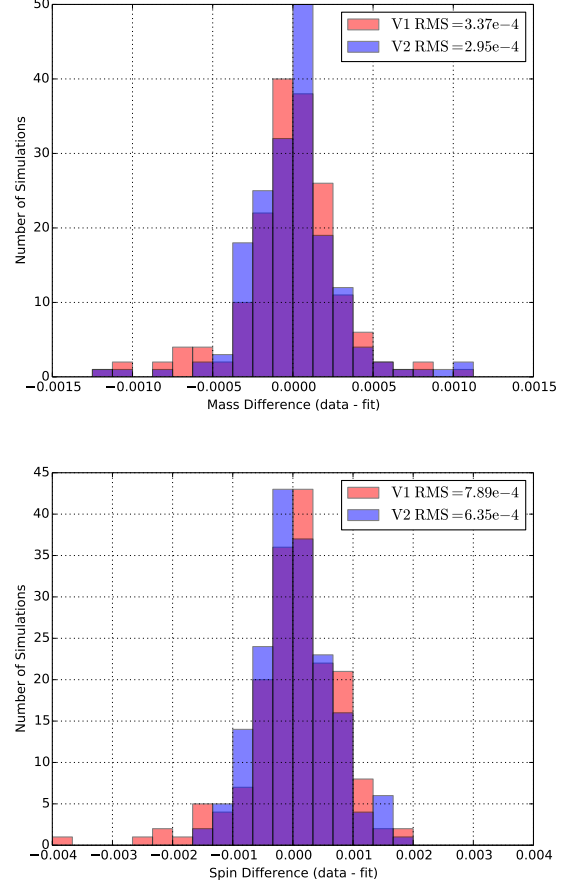


FIG. 2. Counts of the number of runs whose residual (data - fit) falls within a particular bin. Both cases have 25 bins over the visible range with the final mass shown in the top panel, and final spin in the bottom panel. V1 labels the fitting from Ref. [17] and V2 labels the fitting from this paper.

spins are anti-aligned with the orbital angular momentum and maximally spinning. In that case only about 3% of the mass is radiated into gravitational waves with $M_{\text{rem}}(1, -1, -1) = 0.96799$.

A similar analysis for the fits to the final remnant spin is shown in Fig. 4 where the residuals are bounded by $\pm 2 \times 10^{-3}$ and typical percentages differences of less than 0.5% (except for those cases where the final spin is close to zero).

The maximum (minimum) remnant spin are achieved in the particle limit for maximal Kerr aligned (anti-aligned) spinning black holes, but if we consider equal mass binaries then the maximum and minimum final spin of the remnant are $\alpha_{\text{rem}}(1, 1, 1) = 0.95149$ and $\alpha_{\text{rem}}(1, -1, -1) = 0.35771$ where $\alpha_{\text{rem}}(q, \alpha_1, \alpha_2)$.

A final remnant black hole with vanishing spin is also achievable according to these remnant formulae for $q \leq 0.3$ as shown in Fig. 16 of Ref. [17]. The current iteration of the fit does not change this substantially.

The comparative analysis displayed in Fig. 2 of the

TABLE III. Table of fitting parameters for the mass, and spin formulas.

M0	0.951659 ± 0.000022	L0	0.686732 ± 0.000023
K1	-0.051130 ± 0.000131	L1	0.613285 ± 0.000114
K2a	-0.005699 ± 0.000318	L2a	-0.148530 ± 0.000311
K2b	-0.058064 ± 0.000459	L2b	-0.113826 ± 0.000458
K2c	-0.001867 ± 0.000160	L2c	-0.003240 ± 0.000178
K2d	1.995705 ± 0.000292	L2d	0.798011 ± 0.000297
K3a	0.004991 ± 0.001479	L3a	-0.068782 ± 0.001820
K3b	-0.009238 ± 0.000809	L3b	0.001291 ± 0.000442
K3c	-0.120577 ± 0.000769	L3c	-0.078014 ± 0.000674
K3d	0.016417 ± 0.001121	L3d	1.557286 ± 0.001018
K4a	-0.060721 ± 0.002814	L4a	-0.005710 ± 0.001826
K4b	-0.001798 ± 0.000714	L4b	0.005920 ± 0.000612
K4c	0.000654 ± 0.000225	L4c	-0.001706 ± 0.000255
K4d	-0.156626 ± 0.002114	L4d	-0.058882 ± 0.002072
K4e	0.010303 ± 0.001919	L4e	-0.010187 ± 0.001971
K4f	2.978729 ± 0.000691	L4f	0.964445 ± 0.000706
K4g	0.007904 ± 0.001385	L4g	-0.110885 ± 0.001400
K4h	0.000631 ± 0.000409	L4h	-0.006821 ± 0.001316
K4i	0.084478 ± 0.002097	L4i	-0.081648 ± 0.002222

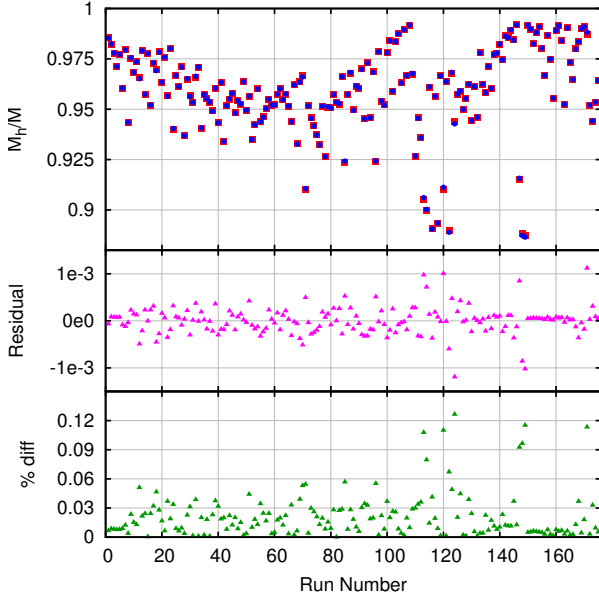


FIG. 3. Predicted values and residuals of the runs compared to the new fitting for the final mass.

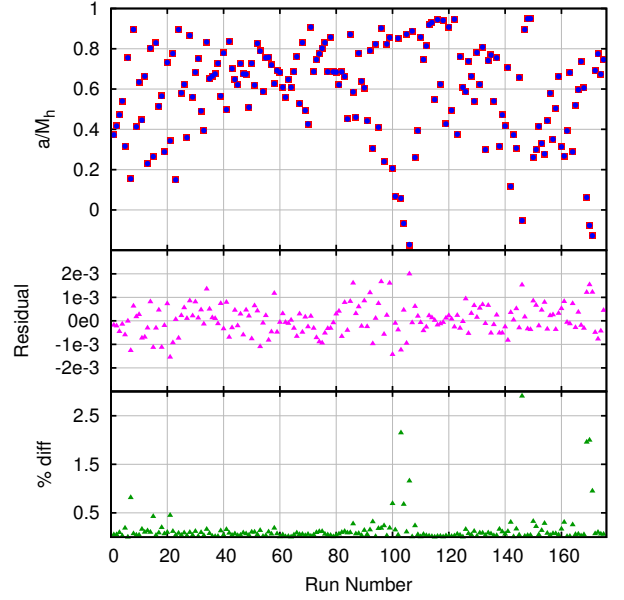


FIG. 4. Predicted values and residuals of the runs compared to the new fitting for the final spin.

old and new formulae shows a slight improvement of the new formulae from the statistical point of view. This improvement is due to a larger (and slightly more accurate) sample of data and the inclusion of relative weights to account for different finite resolutions of the simulations. The improvement is not large in the final mass since the old formula was already providing an excellent approximation. The improvements are more notable for final spin and the recoil velocities, and the newly introduction of a peak luminosity fit as follows in the next subsection.

B. Modeling final Recoils and peak Luminosities

Given the success of the above formulae we will propose a new fitting formula for the peak Luminosity of gravitational waves with a similar form to the mass fitting. The motivation for the above formulae comes from a combination of a Taylor expansion in terms of the seven binary parameters, limited by the symmetry properties of the binary under parity and exchange of the black hole labels. We have also found that the use of the variables \vec{S} , $\vec{\Delta}$, and δm has a direct connection with PN variables

and provides an excellent fit [17, 42, 43, 47]. This can be extended to the peak Luminosity that corresponds to the peak power of gravitational radiation and will share the symmetry properties used for the total final mass of the remnant.

For both the recoil velocity and the peak luminosity fittings we use the original 36 simulations from Ref [17] and the 71 new simulations for a total of 107 simulations.

1. Peak Luminosity fits

We propose

$$L_{\text{peak}} = (4\eta)^2 \left\{ N_0 + N_1 \tilde{S}_{\parallel} + N_{2a} \tilde{\Delta}_{\parallel} \delta m + N_{2b} \tilde{S}_{\parallel}^2 + N_{2c} \tilde{\Delta}_{\parallel}^2 + N_{2d} \delta m^2 + N_{3a} \tilde{\Delta}_{\parallel} \tilde{S}_{\parallel} \delta m + N_{3b} \tilde{S}_{\parallel} \tilde{\Delta}_{\parallel}^2 + N_{3c} \tilde{S}_{\parallel}^3 + N_{3d} \tilde{S}_{\parallel} \delta m^2 + N_{4a} \tilde{\Delta}_{\parallel} \tilde{S}_{\parallel}^2 \delta m + N_{4b} \tilde{\Delta}_{\parallel}^3 \delta m + N_{4c} \tilde{\Delta}_{\parallel}^4 + N_{4d} \tilde{S}_{\parallel}^4 + N_{4e} \tilde{\Delta}_{\parallel}^2 \tilde{S}_{\parallel}^2 + N_{4f} \delta m^4 + N_{4g} \tilde{\Delta}_{\parallel} \delta m^3 + N_{4h} \tilde{\Delta}_{\parallel}^2 \delta m^2 + N_{4i} \tilde{S}_{\parallel}^2 \delta m^2 \right\} (3)$$

Note that the radiated power in the particle limit scales as η^2 (See Ref. [53], Eq. (16) and (20); evaluated at the ISCO for its peak value). Thus we do not include this explicitly in the fitting above, with the same true in the recoil velocity case below.

The best fitted parameters are displayed in Table IV below. The residuals are shown in the top panel of Fig. 5 and the comparison of the fits to data are displayed in Fig. 6. Fig. 6 also displays residuals in the middle panel with values of less than 2×10^{-5} in dimensionless units which corresponds to typical errors of less than 3%.

Note that the percentile errors of the luminosity (and this will also be true for the recoil velocity) are an order of magnitude larger than for the mass and spin of the remnant. This is due to the fact that while the final mass and spin can be obtained very accurately from the isolated horizon formulae applied to the final black hole, the peak luminosity is computed directly from the waveforms at infinity and have errors associated with the finite difference used during the evolution (as well as finite extraction radii and modes used) as detailed in Appendix B. We have used a method of weighted least squares to take into account the different available resolutions for the pool of simulations used in this fit.

By direct evaluation of the fitting formula for the luminosity we see that the maximum value occurs for equal mass binaries and maximum spinning black holes oriented along the orbital angular momentum. In this case we obtain for the peak Luminosity $L_{\text{peak}}(1, 1, 1) = 0.001967$ in dimensionless units, equivalent to $7.1368 \times 10^{56} \text{ ergs/sec}$.

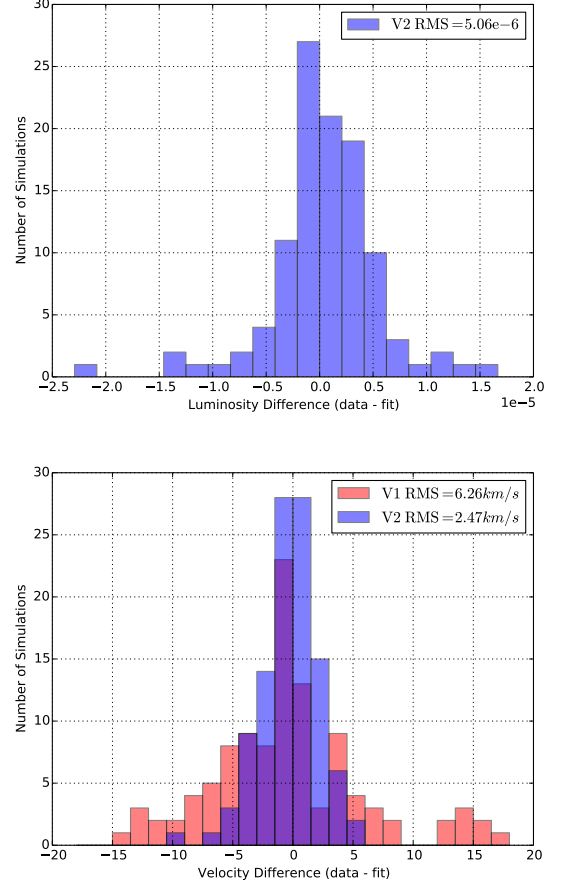


FIG. 5. Counts of the number of runs whose residual (data - fit) falls within a particular bin. Both cases have 25 bins over the visible range with the recoil velocity shown in the top panel, and recoil velocity in the bottom panel. V1 labels the fitting from Ref. [17] and V2 labels the fitting from this paper.

2. Recoil velocities

We model the total recoil as [17]

$$\vec{V}_{\text{recoil}}(q, \vec{\alpha}_i) = v_m \hat{e}_1 + v_{\perp} (\cos(\xi) \hat{e}_1 + \sin(\xi) \hat{e}_2), \quad (4)$$

with,

$$v_{\perp} = H\eta^2 \left(\tilde{\Delta}_{\parallel} + H_{2a} \tilde{S}_{\parallel} \delta m + H_{2b} \tilde{\Delta}_{\parallel} \tilde{S}_{\parallel} + H_{3a} \tilde{\Delta}_{\parallel}^2 \delta m + H_{3b} \tilde{S}_{\parallel}^2 \delta m + H_{3c} \tilde{\Delta}_{\parallel} \tilde{S}_{\parallel}^2 + H_{3d} \tilde{\Delta}_{\parallel}^3 + H_{3e} \tilde{\Delta}_{\parallel} \delta m^2 + H_{4a} \tilde{S}_{\parallel} \tilde{\Delta}_{\parallel}^2 \delta m + H_{4b} \tilde{S}_{\parallel}^3 \delta m + H_{4c} \tilde{S}_{\parallel} \delta m^3 + H_{4d} \tilde{\Delta}_{\parallel} \tilde{S}_{\parallel} \delta m^2 + H_{4e} \tilde{\Delta}_{\parallel} \tilde{S}_{\parallel}^3 + H_{4f} \tilde{S}_{\parallel} \tilde{\Delta}_{\parallel}^3 \right) \quad (5)$$

$$\tilde{\xi} = a + b \tilde{S}_{\parallel} + c \delta m \tilde{\Delta}_{\parallel}.$$

Where

$$v_m = \eta^2 \delta m (A + B \delta m^2). \quad (6)$$

TABLE IV. Table of fitting parameters for the recoil and peak luminosity formulas.

H	$7528.531080 \pm 60.544382$	N0	$1.021017\text{e-}03 \pm 8.905891\text{e-}07$
H2a	-1.795874 ± 0.114360	N1	$8.974289\text{e-}04 \pm 1.892220\text{e-}05$
H2b	-0.615667 ± 0.061626	N2a	$-9.774672\text{e-}05 \pm 4.050598\text{e-}05$
H3a	-0.447651 ± 0.132894	N2b	$9.208838\text{e-}04 \pm 4.258906\text{e-}05$
H3b	-0.771102 ± 0.382234	N2c	$1.869827\text{e-}05 \pm 1.740217\text{e-}05$
H3c	-1.700807 ± 0.177238	N2d	$-3.913170\text{e-}04 \pm 1.368557\text{e-}05$
H3d	-0.021333 ± 0.017638	N3a	$-1.202141\text{e-}04 \pm 1.496747\text{e-}04$
H3e	-0.753230 ± 0.216550	N3b	$1.481022\text{e-}04 \pm 9.213429\text{e-}05$
H4a	-0.585791 ± 0.413974	N3c	$1.379015\text{e-}03 \pm 1.492745\text{e-}04$
H4b	-1.524603 ± 0.929478	N3d	$-4.937306\text{e-}04 \pm 9.776929\text{e-}05$
H4c	0.969809 ± 0.650891	N4a	$8.847927\text{e-}04 \pm 4.470162\text{e-}04$
H4d	0.788852 ± 0.664358	N4b	$3.292542\text{e-}07 \pm 9.428275\text{e-}07$
H4e	-1.701279 ± 0.835741	N4c	$1.701707\text{e-}05 \pm 3.024644\text{e-}05$
H4f	-0.017526 ± 0.224595	N4d	$1.514840\text{e-}03 \pm 2.847964\text{e-}04$
aa	2.463283 ± 0.027020	N4e	$-1.484568\text{e-}04 \pm 1.737503\text{e-}04$
bb	1.466051 ± 0.152762	N4f	$1.366596\text{e-}04 \pm 6.530259\text{e-}05$
cc	0.554279 ± 0.189169	N4g	$1.603431\text{e-}04 \pm 1.673143\text{e-}04$
		N4h	$-6.185306\text{e-}05 \pm 1.113796\text{e-}04$
		N4i	$-1.036025\text{e-}03 \pm 2.504408\text{e-}04$

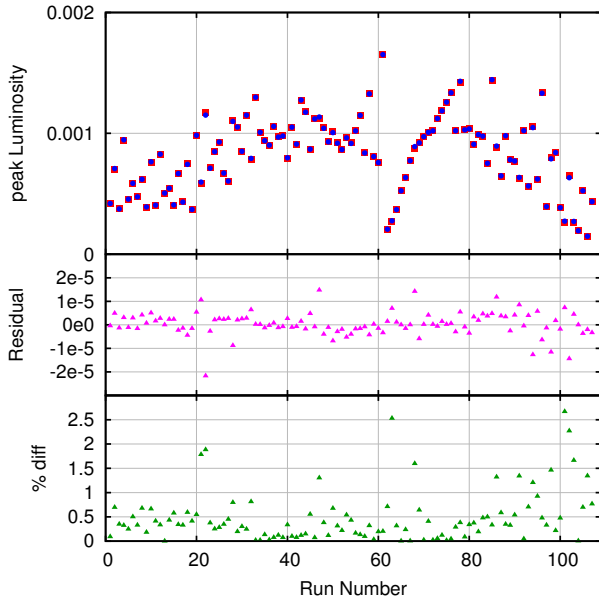


FIG. 6. Predicted values and residuals of the runs compared to the new fitting for the peak Luminosity.

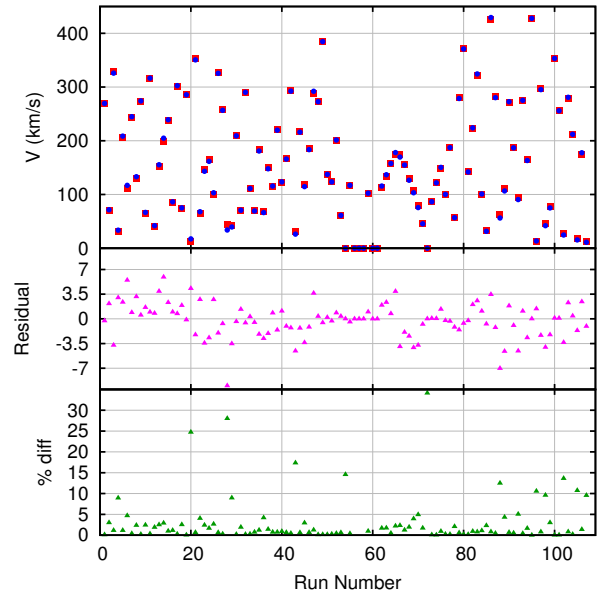


FIG. 7. Predicted values and residuals of the runs compared to the new fitting for the recoil velocity.

and according to Ref. [54] we have $A = 9210 \text{ km/s}$, and $B = 2790 \text{ km/s}$.

In the bottom panel of Fig. 5, the residuals between the first fitting formula and the new fitting formula on the full set of 107 simulations are shown. While the first fitting formula performed reasonably well, with the largest deviations from the data on the order of 15 km/s , the new fitting formula is a marked improvement benefiting from a sample size almost tripled from the first version.

The best fitted parameters are displayed in Table IV below. The comparison of the fits to data are displayed in Fig. 7, that essentially displays residuals of less than

7 km/s , corresponding to typical errors of $5 - 10\%$ for moderate to large recoils.

As for the luminosity, the percentile errors of the recoil velocity are an order of magnitude larger than for the mass and spin of the remnant. We note again that this is due to the fact that while the final mass and spin can be obtained very accurately from the isolated horizon formulae applied to the final black hole, the recoil velocity is computed directly from (different modes of) the waveforms at infinity (See though Ref. [55] for a horizon evaluation of the linear momentum) and have errors associated with the finite difference used during the evolution

(as well as finite extraction radii and modes) as detailed in Appendix B. We have used a method of weighted least squares to take into account the different available resolutions for the pool of simulations used in this fit.

The current analysis with a more extensive set of runs (including the new 71 runs and the former 36 run) allow us to make a statistically more robust determination of the 17 fitting parameters. We can also determine that the maximum recoil velocity does not occur for equal mass binaries but for $q \approx 2/3$ in an up/down configuration. We find $V_{max} = 516.58 \pm 26.33 \text{ km/s}$ for $q_{max} = 0.6628 \pm 0.05661$ with $\alpha_1^{max} = 1.0$ and $\alpha_2^{max} = -1.0$.

In addition to the particle limit and the equal mass, equal spins cases there are other configurations that lead to zero recoil velocity as predicted by the above fitting formulae. We find that the results displayed in Fig. 14 of Ref. [17] is not changed substantially with the updated formulae.

IV. CONCLUSIONS AND DISCUSSION

In this paper we have revisited the scenario of non-precessing binary black hole mergers extending our previous work by tripling the number of simulations. We have thus verified that our formulae for the final remnant mass and spin were accurate well within a fraction of 1% level, and used the new runs to improve those fittings. We observe in the comparative analysis of Fig. 2 that the new fit particularly improves the residuals of the final spin. the residuals now extends nearly half its way and are more symmetric around zero than for the old fit. The improvement is not as evident for the final mass, since the original fit was already extremely good. The comparative analysis of the fittings for the recoil velocity displayed in Fig. 5 shows that the typical residuals are halved by the newly fitted formula. Thus reducing the error of the remnant recoil to within 5%. Finally, we see in the bottom panel of Fig. 6 that the typical residuals of the luminosity fit lie within 2% values. Note that we also improved the assessment of systematic errors in those results by studying the observer location and finite difference dependences of the results, particularly for the recoil velocity and peak luminosity, since the final mass and spin can be obtained more accurately from the horizon evaluated measurements.

These formulae are particularly relevant for LIGO gravitational wave signal analysis. In fact, the formulae of our previous paper [17] has been used to analyze the aLIGO O1 events [5–8, 20, 56]. We expect the implementation of the formulae in this paper (including that of the peak Luminosity) to be used for an improved analysis during the forthcoming aLIGO O2, the second observational run of advanced LIGO.

While the above formulae are strictly valid for non-precessing systems, they represent an important basis to model precessing systems as they provide several of the expansion terms to be included in such formulae

[42, 43, 47] and they represent a reasonable approximation for most applications.

ACKNOWLEDGMENTS

The authors thank M. Campanelli, N.K.Johnson-McDaniel, H. Nakano, R. O’Shaughnessy and Y. Zlochower for discussions on this work. The authors gratefully acknowledge the NSF for financial support from Grants PHY-1607520, PHY-1305730, PHY-1212426, PHY-1229173, AST-1028087, PHY-0969855, OCI-0832606, and DRL-1136221. Computational resources were provided by XSEDE allocation TG-PHY060027N, and by NewHorizons and BlueSky Clusters at Rochester Institute of Technology, which were supported by NSF grant No. PHY-0722703, DMS-0820923, AST-1028087, and PHY-1229173.

Appendix A: Summary of properties of the new simulations

In this appendix, we supplement the initial data parameters given in Tables I-II with more information about the simulations.

In Tables V and VI we give the initial orbital frequency, number of orbits to merger, and initial and final eccentricities measured as [4] $e = r^2 \ddot{r}$.

The values of the individual masses and spins, as well as the recombinations of mass ratio and the two spins used in the fitting functions are given in Tables VII and VIII. These relaxed values are measured at evolution time $t = 150M$, suitably long enough after the start of the merger for the initial ansatz content to settle.

In Tables IX and X, the energy radiated and final spins are given. Both quantities are calculated in two ways, one locally on the isolated horizon, and one from the extrapolation of the gravitational waveforms to infinite observer location. The errors given for the horizon quantities are the drift in the quantity from the value calculated just after merger until the end of the simulation, typically 400–500M evolution time. For the quantities calculated from the gravitational waves, the error is the difference between a first and second order polynomial extrapolation to infinite observer location.

Finally, in Tables XI, XII, and XIII, the recoil velocities and peak luminosities are given. Since the calculation for the kick uses a new method explained below and since the peak luminosities were not given in Paper 1 [17], we provide XIII for the simulations of Paper 1. In this table, we provide both the new run number in the first column, along with the Paper 1 run number in column 2. Error bars for the recoil and luminosity are described in the next appendix.

TABLE V. Table of the initial orbital frequency $m\omega_i$, number of orbits to merger, N , and the initial and final eccentricities, e_i and e_f for the spinning cases.

Run	Config.	$m\omega_i$	N	e_i	e_f
1	Q0.3333_0.0000_-0.5000	0.0236	8.7	0.022	0.002
2	Q0.3333_0.0000_0.5000	0.0269	10.5	0.019	0.002
3	Q0.3333_0.0000_-0.8500	0.0241	7.6	0.016	0.006
4	Q0.3333_0.0000_0.8500	0.0274	12.1	0.019	0.002
5	Q0.3333_-0.5000_-0.2500	0.0226	10.0	0.022	0.001
6	Q0.3333_-0.5000_0.2500	0.0249	10.3	0.020	0.001
7	Q0.3333_0.5000_-0.2500	0.0252	8.9	0.021	0.002
8	Q0.3333_0.5000_0.2500	0.0271	9.7	0.019	0.002
9	Q0.3333_-0.5000_-0.6500	0.0229	8.6	0.017	0.005
10	Q0.3333_-0.5000_0.6500	0.0270	10.8	0.019	0.002
11	Q0.3333_0.5000_-0.6500	0.0244	8.0	0.023	0.003
12	Q0.3333_0.5000_0.6500	0.0275	11.3	0.018	0.003
13	Q0.3333_-0.8000_0.0000	0.0240	9.9	0.015	0.004
14	Q0.3333_0.8000_0.0000	0.0257	10.2	0.016	0.003
15	Q0.3333_-0.8000_-0.5000	0.0228	8.9	0.016	0.005
16	Q0.3333_-0.8000_0.5000	0.0277	9.8	0.010	0.004
17	Q0.3333_0.8000_-0.5000	0.0273	7.5	0.015	0.005
18	Q0.3333_0.8000_0.5000	0.0287	10.6	0.013	0.002
19	Q0.3333_-0.8000_-0.8000	0.0205	9.7	0.018	0.005
20	Q0.3333_0.8000_0.8000	0.0306	11.1	0.012	0.001
21	Q0.5000_0.0000_-0.8000	0.0204	9.6	0.012	0.003
22	Q0.5000_0.0000_0.8000	0.0244	11.9	0.001	0.002
23	Q0.5000_-0.5000_-0.1000	0.0211	10.6	0.027	0.001
24	Q0.5000_0.5000_0.1000	0.0218	12.0	0.008	0.001
25	Q0.5000_-0.5000_0.5000	0.0290	7.6	0.023	0.001
26	Q0.5000_0.5000_-0.5000	0.0273	7.0	0.005	0.004
27	Q0.5000_-0.5000_-0.6000	0.0204	9.6	0.015	0.003
28	Q0.5000_0.5000_0.6000	0.0229	13.1	0.005	0.001
29	Q0.7500_0.0000_0.2500	0.0295	6.8	0.011	0.003
30	Q0.7500_0.0000_-0.5000	0.0278	6.2	0.005	0.005
31	Q0.7500_0.0000_0.5000	0.0258	9.2	0.002	0.003
32	Q0.7500_0.0000_-0.8000	0.0289	5.4	0.006	0.005
33	Q0.7500_0.0000_0.8000	0.0255	10.2	0.001	0.002
34	Q0.7500_-0.2500_0.2500	0.0299	6.3	0.011	0.003
35	Q0.7500_0.2500_-0.2500	0.0302	5.9	0.011	0.003
36	Q0.7500_-0.5000_0.0000	0.0263	6.9	0.002	0.003
37	Q0.7500_0.5000_0.0000	0.0252	8.9	0.000	0.001
38	Q0.7500_-0.5000_0.2500	0.0318	5.7	0.014	0.003
39	Q0.7500_0.5000_-0.2500	0.0297	6.3	0.011	0.002
40	Q0.7500_-0.5000_-0.5000	0.0289	5.3	0.007	0.006
41	Q0.7500_-0.5000_0.5000	0.0264	8.1	0.003	0.004
42	Q0.7500_0.5000_-0.5000	0.0270	7.2	0.004	0.003
43	Q0.7500_0.5000_0.5000	0.0254	10.3	0.002	0.002
44	Q0.7500_-0.5000_0.8000	0.0261	9.1	0.001	0.003
45	Q0.7500_-0.8000_0.0000	0.0281	6.1	0.006	0.005
46	Q0.7500_0.8000_0.0000	0.0258	9.3	0.002	0.003
47	Q0.7500_-0.8000_0.8000	0.0313	6.5	0.021	0.005
48	Q0.7500_-0.8500_0.6375	0.0270	7.8	0.003	0.004
49	Q0.7500_0.8500_-0.6375	0.0271	7.4	0.002	0.002
50	Q0.8200_-0.4400_0.3300	0.0215	10.4	0.031	0.001
51	Q1.0000_0.0000_-0.5000	0.0276	6.4	0.005	0.005
52	Q1.0000_0.0000_-0.8000	0.0285	5.7	0.006	0.002
53	Q1.0000_-0.2500_0.0000	0.0225	9.1	0.010	0.002
54	Q1.0000_-0.2500_-0.2500	0.0228	8.5	0.009	0.002
55	Q1.0000_-0.2500_0.2500	0.0223	9.8	0.010	0.001
56	Q1.0000_0.2500_0.2500	0.0219	11.1	0.011	0.001
57	Q1.0000_-0.5000_-0.5000	0.0289	5.3	0.007	0.007
58	Q1.0000_0.5000_0.5000	0.0248	10.3	0.001	0.001
59	Q1.0000_-0.8000_-0.4000	0.0212	8.4	0.015	0.004
60	Q1.0000_-0.8000_-0.8000	0.0314	4.0	0.018	0.003
61	Q1.0000_0.8000_0.8000	0.0281	9.9	0.007	0.001

TABLE VI. Table of the initial orbital frequency $m\omega_i$, number of orbits to merger, N , and the initial and final eccentricities, e_i and e_f for nonspinning systems.

Run	Config.	$m\omega_i$	N	e_i	e_f
62	Q0.1667_0.0000_0.0000	0.0260	12.6	0.009	0.002
63	Q0.2000_0.0000_0.0000	0.0254	11.4	0.012	0.001
64	Q0.2500_0.0000_0.0000	0.0248	10.8	0.016	0.002
65	Q0.3333_0.0000_0.0000	0.0242	10.1	0.021	0.001
66	Q0.4000_0.0000_0.0000	0.0244	9.4	0.024	0.002
67	Q0.5000_0.0000_0.0000	0.0254	8.4	0.026	0.001
68	Q0.6000_0.0000_0.0000	0.0238	9.1	0.029	0.001
69	Q0.6667_0.0000_0.0000	0.0228	10.0	0.030	0.002
70	Q0.7500_0.0000_0.0000	0.0257	7.9	0.029	0.002
71	Q0.8500_0.0000_0.0000	0.0223	9.9	0.030	0.001

TABLE VII. The mass and spin of the BHBs in Table I after the BHs had time to equilibrate ($t/M = 150$).

Run	Config.	q^r	m_1^r/m	m_2^r/m	α_1^r	α_2^r	δm_r	S_r/m_r^2	Δ_r/m_r^2
1	Q0.3333_0.0000_-0.5000	0.333349	0.250001	0.749967	-0.000002	-0.500063	-0.499982	-0.281279	-0.375042
2	Q0.3333_0.0000_0.5000	0.333349	0.250001	0.749967	-0.000002	0.500054	-0.499982	0.281273	0.375036
3	Q0.3333_0.0000_-0.8500	0.333590	0.250001	0.749425	-0.000002	-0.851337	-0.499711	-0.478692	-0.638379
4	Q0.3333_0.0000_0.8500	0.333588	0.250001	0.749431	-0.000002	0.851293	-0.499713	0.478669	0.638348
5	Q0.3333_-0.5000_-0.2500	0.333346	0.250011	0.750003	-0.500031	-0.250004	-0.499985	-0.171878	-0.062489
6	Q0.3333_-0.5000_0.2500	0.333348	0.250012	0.750003	-0.500027	0.250004	-0.499983	0.109370	0.312512
7	Q0.3333_0.5000_-0.2500	0.333350	0.250013	0.750001	0.499990	-0.250006	-0.499981	-0.109373	-0.312504
8	Q0.3333_0.5000_0.2500	0.333352	0.250014	0.750001	0.499986	0.250006	-0.499979	0.171876	0.062500
9	Q0.3333_-0.5000_-0.6500	0.3333404	0.250010	0.749871	-0.500032	-0.650245	-0.499921	-0.396986	-0.362630
10	Q0.3333_-0.5000_0.6500	0.333407	0.250013	0.749874	-0.500027	0.650224	-0.499917	0.334449	0.612669
11	Q0.3333_0.5000_-0.6500	0.333407	0.250012	0.749871	0.499991	-0.650247	-0.499917	-0.334464	-0.612677
12	Q0.3333_0.5000_0.6500	0.333408	0.250013	0.749873	0.499986	0.650231	-0.499916	0.396974	0.362628
13	Q0.3333_-0.8000_0.0000	0.333237	0.249932	0.750011	-0.800604	0.000006	-0.500108	-0.050013	0.200112
14	Q0.3333_0.8000_0.0000	0.333247	0.249936	0.750002	0.800511	0.000002	-0.500097	0.050013	-0.200088
15	Q0.3333_-0.8000_-0.5000	0.333250	0.249930	0.749976	-0.800619	-0.500032	-0.500094	-0.331323	-0.174930
16	Q0.3333_-0.8000_0.5000	0.333261	0.249939	0.749980	-0.800553	0.500026	-0.500082	0.231277	0.575146
17	Q0.3333_0.8000_-0.5000	0.333265	0.249938	0.749969	0.800473	-0.500055	-0.500077	-0.231296	-0.575148
18	Q0.3333_0.8000_0.5000	0.333267	0.249940	0.749969	0.800454	0.500050	-0.500074	0.331319	0.174972
19	Q0.3333_-0.8000_-0.8000	0.333408	0.249924	0.749603	-0.800648	-0.800863	-0.499916	-0.500492	-0.400418
20	Q0.3333_0.8000_0.8000	0.333432	0.249943	0.749607	0.800410	0.800846	-0.499889	0.500457	0.400443
21	Q0.5000_0.0000_-0.8000	0.500261	0.333334	0.666320	-0.000002	-0.800844	-0.333102	-0.355807	-0.533803
22	Q0.5000_0.0000_0.8000	0.500256	0.333333	0.666326	-0.000001	0.800792	-0.333106	0.355786	0.533771
23	Q0.5000_-0.5000_-0.1000	0.500006	0.333338	0.666668	-0.500052	-0.100003	-0.333328	-0.100008	0.100017
24	Q0.5000_0.5000_0.1000	0.500007	0.333338	0.666667	0.500025	0.100004	-0.333327	0.100005	-0.100008
25	Q0.5000_-0.5000_0.5000	0.500031	0.333345	0.666648	-0.500013	0.500027	-0.333306	0.166664	0.500022
26	Q0.5000_0.5000_-0.5000	0.500030	0.333342	0.666643	0.500035	-0.500063	-0.333307	-0.166678	-0.500054
27	Q0.5000_-0.5000_-0.6000	0.500059	0.333338	0.666597	-0.500051	-0.600147	-0.333281	-0.322281	-0.233386
28	Q0.5000_0.5000_0.6000	0.500061	0.333339	0.666596	0.500024	0.600134	-0.333279	0.322272	0.233385
29	Q0.7500_0.0000_0.2500	0.749995	0.428572	0.571433	-0.000002	0.249997	-0.142860	0.081632	0.142857
30	Q0.7500_0.0000_-0.5000	0.750017	0.428572	0.571416	-0.000002	-0.500049	-0.142846	-0.163278	-0.285738
31	Q0.7500_0.0000_0.5000	0.750018	0.428571	0.571415	-0.000001	0.500028	-0.142846	0.163271	0.285728
32	Q0.7500_0.0000_-0.8000	0.750353	0.428575	0.571164	-0.000001	-0.800786	-0.142627	-0.261376	-0.457499
33	Q0.7500_0.0000_0.8000	0.750355	0.428572	0.571159	-0.000001	0.800755	-0.142625	0.261365	0.457482
34	Q0.7500_-0.2500_0.2500	0.750005	0.428577	0.571433	-0.250008	0.249996	-0.142854	0.035711	0.250002
35	Q0.7500_0.2500_-0.2500	0.750006	0.428578	0.571433	0.249993	-0.250006	-0.142853	-0.035716	-0.250000
36	Q0.7500_-0.5000_0.0000	0.750001	0.428573	0.571430	-0.500036	-0.000000	-0.142856	-0.091844	0.214301
37	Q0.7500_0.5000_0.0000	0.750002	0.428572	0.571428	0.500007	-0.000000	-0.142856	0.091838	-0.214289
38	Q0.7500_-0.5000_0.2500	0.750000	0.428576	0.571435	-0.500031	0.249993	-0.142857	-0.010212	0.357152
39	Q0.7500_0.5000_-0.2500	0.750004	0.428576	0.571433	0.499989	-0.250006	-0.142855	0.010201	-0.357142
40	Q0.7500_-0.5000_-0.5000	0.750019	0.428575	0.571419	-0.500031	-0.500038	-0.142845	-0.255119	-0.071431
41	Q0.7500_-0.5000_0.5000	0.750016	0.428572	0.571418	-0.500038	0.500021	-0.142847	0.071423	0.500028
42	Q0.7500_0.5000_-0.5000	0.750021	0.428573	0.571415	0.500002	-0.500050	-0.142844	-0.071438	-0.500029
43	Q0.7500_0.5000_0.5000	0.750018	0.428571	0.571414	0.500010	0.500029	-0.142845	0.255112	0.071435
44	Q0.7500_-0.5000_0.8000	0.750351	0.428572	0.571162	-0.500035	0.800741	-0.142628	0.169469	0.671832
45	Q0.7500_-0.8000_0.0000	0.749701	0.428408	0.571439	-0.800681	0.000002	-0.143053	-0.146996	0.343072
46	Q0.7500_0.8000_0.0000	0.749704	0.428403	0.571430	0.800634	-0.000000	-0.143051	0.146989	-0.343052
47	Q0.7500_-0.8000_0.8000	0.750044	0.428413	0.571185	-0.800638	0.800638	-0.142829	0.114354	0.800638
48	Q0.7500_-0.8500_0.6375	0.749627	0.428318	0.571375	-0.851092	0.637601	-0.143101	0.052051	0.729071
49	Q0.7500_0.8500_-0.6375	0.749648	0.428321	0.571363	0.850998	-0.637676	-0.143087	-0.052082	-0.729075
50	Q0.8200_-0.4400_0.3300	0.819999	0.450552	0.549454	-0.440020	0.329999	-0.098902	0.010304	0.379569
51	Q1.0000_0.0000_-0.5000	1.000013	0.499999	0.499992	-0.000001	-0.499978	0.000007	-0.124993	-0.249987
52	Q1.0000_0.0000_-0.8000	1.000437	0.500005	0.499787	-0.000001	-0.800758	0.000219	-0.200102	-0.400291
53	Q1.0000_-0.2500_0.0000	1.000008	0.500001	0.499997	-0.249958	-0.000001	0.000004	-0.062490	0.124979
54	Q1.0000_-0.2500_-0.2500	1.000000	0.500001	0.500001	-0.249958	-0.249958	0.000000	-0.124979	0.000000
55	Q1.0000_-0.2500_0.2500	1.000000	0.500001	0.500001	-0.249958	0.249950	-0.000000	-0.000002	0.249954
56	Q1.0000_0.2500_0.2500	1.000000	0.500001	0.500001	0.249950	0.249950	-0.000000	0.124975	0.000000
57	Q1.0000_-0.5000_-0.5000	1.000000	0.499994	0.499994	-0.499971	-0.499972	-0.000000	-0.249986	-0.000000
58	Q1.0000_0.5000_0.5000	1.000000	0.499991	0.499991	0.499953	0.499953	-0.000000	0.249976	0.000000
59	Q1.0000_-0.8000_-0.4000	0.999539	0.499773	0.500004	-0.800796	-0.399931	-0.000230	-0.300136	0.200295
60	Q1.0000_-0.8000_0.8000	1.000000	0.499794	0.499794	-0.800705	-0.800705	-0.000000	-0.400353	-0.000000
61	Q1.0000_0.8000_0.8000	1.000000	0.499788	0.499788	0.800682	0.800682	-0.000000	0.400341	0.000000

TABLE VIII. The mass and spin of the BHBs in Table I after the BHs had time to equilibrate ($t/M = 150$) for non-spinning systems.

Run	Config.	q^r	m_1^r/m	m_2^r/m	α_1^r	α_2^r	δm_r	S_r/m_r^2	Δ_r/m_r^2
62	Q0.1667_0.0000_0.0000	0.166674	0.142863	0.857142	0.000008	0.000001	-0.714275	0.000001	-0.000000
63	Q0.2000_0.0000_0.0000	0.200005	0.166671	0.833333	-0.000001	0.000001	-0.666659	0.000001	0.000001
64	Q0.2500_0.0000_0.0000	0.250002	0.200001	0.800000	-0.000002	0.000001	-0.599998	0.000000	0.000001
65	Q0.3333_0.0000_0.0000	0.333335	0.250001	0.750000	-0.000002	0.000000	-0.499998	0.000000	0.000001
66	Q0.4000_0.0000_0.0000	0.400005	0.285718	0.714286	-0.000003	0.000000	-0.428566	-0.000000	0.000001
67	Q0.5000_0.0000_0.0000	0.500001	0.333334	0.666667	-0.000002	-0.000000	-0.333333	-0.000000	0.000001
68	Q0.6000_0.0000_0.0000	0.600000	0.374999	0.624999	-0.000001	-0.000000	-0.250000	-0.000000	0.000000
69	Q0.6667_0.0000_0.0000	0.666687	0.400011	0.599999	-0.000006	-0.000000	-0.199986	-0.000001	0.000002
70	Q0.7500_0.0000_0.0000	0.750011	0.428578	0.571429	-0.000001	-0.000001	-0.142850	-0.000000	0.000000
71	Q0.8500_0.0000_0.0000	0.850013	0.459467	0.540541	0.000001	-0.000001	-0.081073	0.000000	-0.000001

TABLE IX. The final energy radiated and spin as measured using the IH formalism and as measured from the radiation of energy and angular momentum. The error bars in the radiative quantities are due to radial extrapolation errors while the error bars in the IH quantities are due to variations in the measured mass and spin with time.

Run	Config.	$\delta\mathcal{M}^{IH}$	$\delta\mathcal{M}^{rad}$	α_{rem}^{IH}	α_{rem}^{rad}
1	Q0.3333_0.0000_-0.5000	0.022851 \pm 0.000002	0.022817 \pm 0.000135	0.316214 \pm 0.000003	0.313624 \pm 0.006158
2	Q0.3333_0.0000_0.5000	0.039597 \pm 0.000001	0.039168 \pm 0.000145	0.755227 \pm 0.000063	0.753742 \pm 0.005431
3	Q0.3333_0.0000_-0.8500	0.020650 \pm 0.000002	0.020650 \pm 0.000166	0.154585 \pm 0.000007	0.152043 \pm 0.006126
4	Q0.3333_0.0000_0.8500	0.056496 \pm 0.000000	0.055113 \pm 0.000476	0.895880 \pm 0.000003	0.895066 \pm 0.007610
5	Q0.3333_-0.5000_-0.2500	0.024450 \pm 0.000004	0.024341 \pm 0.000149	0.412707 \pm 0.000003	0.409940 \pm 0.007081
6	Q0.3333_-0.5000_0.2500	0.031700 \pm 0.000000	0.031438 \pm 0.000128	0.634229 \pm 0.000006	0.632239 \pm 0.005915
7	Q0.3333_0.5000_-0.2500	0.026411 \pm 0.000001	0.026301 \pm 0.000105	0.445700 \pm 0.000006	0.443547 \pm 0.005283
8	Q0.3333_0.5000_0.2500	0.034833 \pm 0.000003	0.034557 \pm 0.000093	0.664090 \pm 0.000002	0.662470 \pm 0.004798
9	Q0.3333_-0.5000_-0.6500	0.020982 \pm 0.000000	0.020936 \pm 0.000159	0.230000 \pm 0.000008	0.227124 \pm 0.006786
10	Q0.3333_-0.5000_0.6500	0.042569 \pm 0.000000	0.041919 \pm 0.000216	0.803309 \pm 0.000047	0.801973 \pm 0.005941
11	Q0.3333_0.5000_-0.6500	0.022422 \pm 0.000000	0.022373 \pm 0.000138	0.264943 \pm 0.000007	0.262435 \pm 0.005705
12	Q0.3333_0.5000_0.6500	0.048004 \pm 0.000001	0.047242 \pm 0.000229	0.829632 \pm 0.000030	0.828412 \pm 0.005938
13	Q0.3333_-0.8000_0.0000	0.026981 \pm 0.000003	0.026649 \pm 0.000137	0.514639 \pm 0.000005	0.513271 \pm 0.006530
14	Q0.3333_0.8000_0.0000	0.030886 \pm 0.000002	0.030531 \pm 0.000114	0.565067 \pm 0.000005	0.563548 \pm 0.005781
15	Q0.3333_-0.8000_-0.5000	0.021678 \pm 0.000000	0.021448 \pm 0.000155	0.288018 \pm 0.000003	0.286577 \pm 0.006891
16	Q0.3333_-0.8000_0.5000	0.036549 \pm 0.000003	0.035953 \pm 0.000151	0.732134 \pm 0.000024	0.731806 \pm 0.005237
17	Q0.3333_0.8000_-0.5000	0.024281 \pm 0.000001	0.024037 \pm 0.000107	0.342874 \pm 0.000001	0.341834 \pm 0.004626
18	Q0.3333_0.8000_0.5000	0.043435 \pm 0.000005	0.042744 \pm 0.000148	0.776618 \pm 0.000134	0.776230 \pm 0.005133
19	Q0.3333_-0.8000_-0.8000	0.019848 \pm 0.000002	0.019659 \pm 0.000218	0.149516 \pm 0.000003	0.147452 \pm 0.008868
20	Q0.3333_0.8000_0.8000	0.059611 \pm 0.000125	0.057982 \pm 0.000431	0.894974 \pm 0.002397	0.895480 \pm 0.006129
21	Q0.5000_0.0000_-0.8000	0.029011 \pm 0.000005	0.028849 \pm 0.000308	0.359268 \pm 0.000005	0.354958 \pm 0.011629
22	Q0.5000_0.0000_0.8000	0.063041 \pm 0.000000	0.060434 \pm 0.000791	0.865799 \pm 0.000107	0.865719 \pm 0.012199
23	Q0.5000_-0.5000_-0.1000	0.034843 \pm 0.000003	0.034440 \pm 0.000276	0.560690 \pm 0.000018	0.557023 \pm 0.011230
24	Q0.5000_0.5000_0.1000	0.043650 \pm 0.000004	0.042936 \pm 0.000332	0.683753 \pm 0.000143	0.680628 \pm 0.011798
25	Q0.5000_-0.5000_0.5000	0.046664 \pm 0.000001	0.046314 \pm 0.000143	0.750834 \pm 0.000003	0.748841 \pm 0.005544
26	Q0.5000_0.5000_-0.5000	0.033650 \pm 0.000002	0.033372 \pm 0.000165	0.491246 \pm 0.000001	0.489202 \pm 0.006112
27	Q0.5000_-0.5000_-0.6000	0.029090 \pm 0.000000	0.028893 \pm 0.000274	0.394301 \pm 0.000002	0.390023 \pm 0.011285
28	Q0.5000_0.5000_0.6000	0.059275 \pm 0.000001	0.057310 \pm 0.000639	0.833826 \pm 0.000020	0.832455 \pm 0.013082
29	Q0.7500_0.0000_-0.2500	0.051049 \pm 0.000001	0.050317 \pm 0.000218	0.727731 \pm 0.000003	0.726413 \pm 0.006203
30	Q0.7500_0.0000_-0.5000	0.039526 \pm 0.000001	0.039233 \pm 0.000180	0.566042 \pm 0.000006	0.563686 \pm 0.006655
31	Q0.7500_0.0000_0.5000	0.056774 \pm 0.000001	0.055687 \pm 0.000356	0.778674 \pm 0.000001	0.776580 \pm 0.009746
32	Q0.7500_0.0000_-0.8000	0.036685 \pm 0.000000	0.036378 \pm 0.000215	0.498004 \pm 0.000005	0.496150 \pm 0.006218
33	Q0.7500_0.0000_0.8000	0.066017 \pm 0.000000	0.064170 \pm 0.000608	0.836975 \pm 0.000040	0.835320 \pm 0.011812
34	Q0.7500_-0.2500_0.2500	0.048311 \pm 0.000001	0.047681 \pm 0.000204	0.701752 \pm 0.000005	0.700428 \pm 0.005855
35	Q0.7500_0.2500_-0.2500	0.044884 \pm 0.000001	0.044437 \pm 0.000173	0.647887 \pm 0.000004	0.646394 \pm 0.005491
36	Q0.7500_-0.5000_0.0000	0.042106 \pm 0.000001	0.041679 \pm 0.000197	0.621030 \pm 0.000006	0.618628 \pm 0.007280
37	Q0.7500_0.5000_0.0000	0.051985 \pm 0.000002	0.051220 \pm 0.000280	0.726504 \pm 0.000002	0.723901 \pm 0.009257
38	Q0.7500_-0.5000_0.2500	0.045826 \pm 0.000001	0.045255 \pm 0.000200	0.674934 \pm 0.000007	0.673806 \pm 0.005391
39	Q0.7500_0.5000_-0.2500	0.047349 \pm 0.000001	0.046807 \pm 0.000199	0.673966 \pm 0.000005	0.672384 \pm 0.005937
40	Q0.7500_-0.5000_-0.5000	0.036361 \pm 0.000001	0.036099 \pm 0.000171	0.509444 \pm 0.000007	0.507455 \pm 0.005885
41	Q0.7500_-0.5000_0.5000	0.050463 \pm 0.000000	0.049660 \pm 0.000300	0.727625 \pm 0.000002	0.725455 \pm 0.008693
42	Q0.7500_0.5000_-0.5000	0.043506 \pm 0.000000	0.043094 \pm 0.000222	0.619960 \pm 0.000001	0.617349 \pm 0.007628
43	Q0.7500_0.5000_0.5000	0.065024 \pm 0.000001	0.063390 \pm 0.000506	0.826599 \pm 0.000017	0.824800 \pm 0.011315
44	Q0.7500_-0.5000_0.8000	0.057720 \pm 0.000001	0.056416 \pm 0.000482	0.788343 \pm 0.000002	0.786306 \pm 0.010466
45	Q0.7500_-0.8000_0.0000	0.039962 \pm 0.000002	0.039397 \pm 0.000213	0.587671 \pm 0.000007	0.586076 \pm 0.006659
46	Q0.7500_0.8000_0.0000	0.056197 \pm 0.000002	0.055082 \pm 0.000370	0.755757 \pm 0.000010	0.753416 \pm 0.009901
47	Q0.7500_-0.8000_0.8000	0.053885 \pm 0.000005	0.053426 \pm 0.000254	0.757809 \pm 0.000006	0.755944 \pm 0.006548
48	Q0.7500_-0.8500_0.6375	0.049693 \pm 0.000001	0.048605 \pm 0.000372	0.719449 \pm 0.000003	0.717813 \pm 0.008919
49	Q0.7500_0.8500_-0.6375	0.045036 \pm 0.000001	0.044326 \pm 0.000316	0.626888 \pm 0.000000	0.624688 \pm 0.008358
50	Q0.8200_-0.4400_0.3300	0.047979 \pm 0.000002	0.047775 \pm 0.000268	0.691971 \pm 0.000001	0.686578 \pm 0.012997
51	Q1.0000_0.0000_-0.5000	0.042523 \pm 0.000001	0.042147 \pm 0.000192	0.608514 \pm 0.000019	0.606031 \pm 0.007032
52	Q1.0000_0.0000_-0.8000	0.039828 \pm 0.000002	0.039387 \pm 0.000229	0.559265 \pm 0.000007	0.557558 \pm 0.006678
53	Q1.0000_-0.2500_0.0000	0.045246 \pm 0.000003	0.044786 \pm 0.000275	0.647826 \pm 0.000038	0.643983 \pm 0.011363
54	Q1.0000_-0.2500_-0.2500	0.042447 \pm 0.000005	0.042077 \pm 0.000251	0.608476 \pm 0.000019	0.604880 \pm 0.010617
55	Q1.0000_-0.2500_0.2500	0.048423 \pm 0.000005	0.047841 \pm 0.000315	0.686208 \pm 0.000087	0.682593 \pm 0.012264
56	Q1.0000_0.2500_0.2500	0.056224 \pm 0.000010	0.055271 \pm 0.000410	0.760776 \pm 0.000413	0.758590 \pm 0.013925
57	Q1.0000_-0.5000_-0.5000	0.037937 \pm 0.000002	0.037667 \pm 0.000179	0.527590 \pm 0.000016	0.525104 \pm 0.006089
58	Q1.0000_0.5000_0.5000	0.067306 \pm 0.000009	0.065641 \pm 0.000523	0.830996 \pm 0.000268	0.829616 \pm 0.011876
59	Q1.0000_-0.8000_-0.4000	0.036537 \pm 0.000004	0.036165 \pm 0.000325	0.494027 \pm 0.000013	0.489738 \pm 0.012360
60	Q1.0000_-0.8000_0.8000	0.033977 \pm 0.000003	0.033485 \pm 0.000243	0.426200 \pm 0.000026	0.425451 \pm 0.005243
61	Q1.0000_0.8000_0.8000	0.089381 \pm 0.000075	0.085140 \pm 0.001195	0.907691 \pm 0.000042	0.908899 \pm 0.013099

TABLE X. The final energy radiated and spin as measured using the IH formalism and as measured from the radiation of energy and angular momentum. Same as in Table IX but for non-spinning systems.

Run	Config.	$\delta\mathcal{M}^{IH}$	$\delta\mathcal{M}^{rad}$	α_{rem}^{IH}	α_{rem}^{rad}
62	Q0.1667_0.0000_0.0000	0.014711 ± 0.000008	0.014558 ± 0.000083	0.372243 ± 0.000024	0.366107 ± 0.003115
63	Q0.2000_0.0000_0.0000	0.017650 ± 0.000004	0.017461 ± 0.000094	0.416663 ± 0.000014	0.414855 ± 0.003649
64	Q0.2500_0.0000_0.0000	0.022082 ± 0.000004	0.021860 ± 0.000115	0.471618 ± 0.000002	0.470320 ± 0.004711
65	Q0.3333_0.0000_0.0000	0.028719 ± 0.000001	0.028582 ± 0.000120	0.540600 ± 0.000003	0.538311 ± 0.006163
66	Q0.4000_0.0000_0.0000	0.033245 ± 0.000002	0.032988 ± 0.000157	0.580738 ± 0.000014	0.579238 ± 0.006950
67	Q0.5000_0.0000_0.0000	0.038747 ± 0.000000	0.038616 ± 0.000122	0.623456 ± 0.000000	0.620479 ± 0.006881
68	Q0.6000_0.0000_0.0000	0.042781 ± 0.000002	0.042496 ± 0.000206	0.651373 ± 0.000010	0.647754 ± 0.009099
69	Q0.6667_0.0000_0.0000	0.044916 ± 0.000018	0.044685 ± 0.000254	0.663910 ± 0.000102	0.650408 ± 0.011148
70	Q0.7500_0.0000_0.0000	0.046490 ± 0.000003	0.046360 ± 0.000139	0.675108 ± 0.000040	0.671341 ± 0.007807
71	Q0.8500_0.0000_0.0000	0.047783 ± 0.000004	0.047488 ± 0.000273	0.682891 ± 0.000041	0.676581 ± 0.012176

TABLE XI. The recoil velocity and peak luminosity as calculated using $\ell_{max} = 6$ and $r_{max} = 113.0M$ for spinning systems. The error estimates are detailed in Appendix B.

Run	Config.	V	\mathcal{L}_{max}
1	Q0.3333_0.0000_-0.5000	269.61 \pm 6.64	4.1989e-04 \pm 5.3772e-06
2	Q0.3333_0.0000_0.5000	71.54 \pm 9.65	7.0865e-04 \pm 1.0874e-05
3	Q0.3333_0.0000_-0.8500	325.83 \pm 6.40	3.7435e-04 \pm 5.3254e-06
4	Q0.3333_0.0000_0.8500	33.54 \pm 6.73	9.4661e-04 \pm 2.3307e-05
5	Q0.3333_-0.5000_-0.2500	208.71 \pm 6.99	4.5570e-04 \pm 5.9348e-06
6	Q0.3333_-0.5000_0.2500	117.02 \pm 8.86	5.8663e-04 \pm 7.3102e-06
7	Q0.3333_0.5000_-0.2500	244.89 \pm 6.80	4.7481e-04 \pm 6.0819e-06
8	Q0.3333_0.5000_0.2500	133.17 \pm 7.94	6.1982e-04 \pm 6.5282e-06
9	Q0.3333_-0.5000_-0.6500	274.13 \pm 6.54	3.9091e-04 \pm 5.5952e-06
10	Q0.3333_-0.5000_0.6500	66.68 \pm 8.57	7.6508e-04 \pm 1.2352e-05
11	Q0.3333_0.5000_-0.6500	316.55 \pm 6.44	4.0568e-04 \pm 5.4250e-06
12	Q0.3333_0.5000_0.6500	41.86 \pm 9.39	8.2784e-04 \pm 1.3973e-05
13	Q0.3333_-0.8000_0.0000	155.41 \pm 7.85	5.0570e-04 \pm 5.8644e-06
14	Q0.3333_0.8000_0.0000	204.93 \pm 7.00	5.4590e-04 \pm 6.0256e-06
15	Q0.3333_-0.8000_-0.5000	239.24 \pm 6.66	4.0786e-04 \pm 5.3643e-06
16	Q0.3333_-0.8000_0.5000	86.30 \pm 8.89	6.6698e-04 \pm 8.4126e-06
17	Q0.3333_0.8000_-0.5000	302.56 \pm 6.57	4.3127e-04 \pm 5.3695e-06
18	Q0.3333_0.8000_0.5000	75.11 \pm 8.56	7.4376e-04 \pm 1.1449e-05
19	Q0.3333_-0.8000_-0.8000	285.61 \pm 6.40	3.6999e-04 \pm 5.2712e-06
20	Q0.3333_0.8000_0.8000	17.42 \pm 9.22	9.8382e-04 \pm 2.2248e-05
21	Q0.5000_0.0000_-0.8000	350.67 \pm 9.36	5.9661e-04 \pm 1.5332e-05
22	Q0.5000_0.0000_0.8000	67.84 \pm 13.08	1.1511e-03 \pm 4.7746e-05
23	Q0.5000_-0.5000_-0.1000	143.24 \pm 13.32	7.1138e-04 \pm 1.9643e-05
24	Q0.5000_0.5000_0.1000	161.66 \pm 11.04	8.4802e-04 \pm 2.4327e-05
25	Q0.5000_-0.5000_0.5000	103.20 \pm 8.11	9.2813e-04 \pm 8.2967e-06
26	Q0.5000_0.5000_-0.5000	325.60 \pm 9.74	6.7153e-04 \pm 1.7319e-05
27	Q0.5000_-0.5000_-0.6000	256.73 \pm 9.98	6.0546e-04 \pm 1.6035e-05
28	Q0.5000_0.5000_0.6000	33.80 \pm 14.28	1.0987e-03 \pm 4.4638e-05
29	Q0.7500_0.0000_0.2500	39.43 \pm 9.87	1.0528e-03 \pm 2.5374e-05
30	Q0.7500_0.0000_-0.5000	209.16 \pm 6.89	8.5126e-04 \pm 1.9985e-05
31	Q0.7500_0.0000_0.5000	70.63 \pm 8.17	1.1504e-03 \pm 3.1034e-05
32	Q0.7500_0.0000_-0.8000	290.22 \pm 6.86	7.9256e-04 \pm 1.9752e-05
33	Q0.7500_0.0000_0.8000	111.17 \pm 7.82	1.2986e-03 \pm 3.9935e-05
34	Q0.7500_-0.2500_0.2500	69.35 \pm 8.64	1.0087e-03 \pm 2.3390e-05
35	Q0.7500_0.2500_-0.2500	180.96 \pm 7.00	9.3926e-04 \pm 2.1835e-05
36	Q0.7500_-0.5000_0.0000	66.33 \pm 8.86	9.0246e-04 \pm 2.0991e-05
37	Q0.7500_0.5000_0.0000	147.79 \pm 6.99	1.0580e-03 \pm 2.3716e-05
38	Q0.7500_-0.5000_0.2500	115.68 \pm 8.04	9.6913e-04 \pm 2.3444e-05
39	Q0.7500_0.5000_-0.2500	219.82 \pm 7.00	9.7811e-04 \pm 2.2179e-05
40	Q0.7500_-0.5000_-0.5000	123.51 \pm 7.07	7.9779e-04 \pm 1.9923e-05
41	Q0.7500_-0.5000_0.5000	166.02 \pm 7.93	1.0512e-03 \pm 2.4317e-05
42	Q0.7500_0.5000_-0.5000	292.56 \pm 6.92	9.1151e-04 \pm 2.1213e-05
43	Q0.7500_0.5000_0.5000	26.22 \pm 8.41	1.2761e-03 \pm 3.4943e-05
44	Q0.7500_-0.5000_0.8000	216.06 \pm 8.01	1.1755e-03 \pm 2.9614e-05
45	Q0.7500_-0.8000_0.0000	114.57 \pm 8.24	8.6890e-04 \pm 2.0880e-05
46	Q0.7500_0.8000_0.0000	183.55 \pm 6.95	1.1198e-03 \pm 2.5957e-05
47	Q0.7500_-0.8000_0.8000	292.19 \pm 6.82	1.1351e-03 \pm 1.9390e-05
48	Q0.7500_-0.8500_0.6375	272.78 \pm 8.32	1.0419e-03 \pm 2.3762e-05
49	Q0.7500_0.8500_-0.6375	384.71 \pm 7.01	9.2953e-04 \pm 2.1158e-05
50	Q0.8200_-0.4400_0.3300	137.44 \pm 1.12	1.0064e-03 \pm 1.9440e-05
51	Q1.0000_0.0000_-0.5000	123.50 \pm 2.90	9.1795e-04 \pm 1.1027e-05
52	Q1.0000_0.0000_-0.8000	201.51 \pm 2.95	8.6553e-04 \pm 1.0178e-05
53	Q1.0000_-0.2500_0.0000	61.05 \pm 2.84	9.6316e-04 \pm 1.2909e-05
54	Q1.0000_-0.2500_-0.2500	0.00 \pm 0.00	9.1696e-04 \pm 1.1294e-05
55	Q1.0000_-0.2500_0.2500	117.02 \pm 2.89	1.0206e-03 \pm 1.3936e-05
56	Q1.0000_0.2500_0.2500	0.00 \pm 0.00	1.1491e-03 \pm 1.9549e-05
57	Q1.0000_-0.5000_-0.5000	0.00 \pm 0.00	8.3778e-04 \pm 9.3235e-06
58	Q1.0000_0.5000_0.5000	0.00 \pm 0.00	1.3261e-03 \pm 3.2405e-05
59	Q1.0000_-0.8000_-0.4000	102.37 \pm 2.84	8.0836e-04 \pm 9.2692e-06
60	Q1.0000_-0.8000_-0.8000	0.00 \pm 0.00	7.5828e-04 \pm 8.8100e-06
61	Q1.0000_0.8000_0.8000	0.00 \pm 0.00	1.6519e-03 \pm 7.2878e-05

TABLE XII. Recoil velocities and peak luminosities as in Table XI but for non-spinning systems.

Run	Config.	V	\mathcal{L}_{\max}
62	Q0.1667_0.0000_0.0000	115.83 ± 6.91	$2.0707\text{e-}04 \pm 8.6305\text{e-}06$
63	Q0.2000_0.0000_0.0000	136.73 ± 7.39	$2.7679\text{e-}04 \pm 7.9392\text{e-}06$
64	Q0.2500_0.0000_0.0000	157.63 ± 8.66	$3.6893\text{e-}04 \pm 8.7373\text{e-}06$
65	Q0.3333_0.0000_0.0000	178.05 ± 7.38	$5.2412\text{e-}04 \pm 6.1042\text{e-}06$
66	Q0.4000_0.0000_0.0000	169.62 ± 6.04	$6.3407\text{e-}04 \pm 6.6580\text{e-}06$
67	Q0.5000_0.0000_0.0000	154.81 ± 5.07	$7.7375\text{e-}04 \pm 1.6389\text{e-}06$
68	Q0.6000_0.0000_0.0000	126.43 ± 7.56	$8.9059\text{e-}04 \pm 3.5371\text{e-}05$
69	Q0.6667_0.0000_0.0000	103.31 ± 5.49	$9.2086\text{e-}04 \pm 6.3996\text{e-}06$
70	Q0.7500_0.0000_0.0000	75.66 ± 1.93	$9.7238\text{e-}04 \pm 1.7329\text{e-}06$
71	Q0.8500_0.0000_0.0000	45.38 ± 3.82	$1.0092\text{e-}03 \pm 1.1205\text{e-}05$

TABLE XIII. Recoil velocities and peak luminosities as in Table XI but for systems in Paper 1 [17] calculated using the new method.

Run	Paper1 Run	Config.	V	\mathcal{L}_{\max}
72	1	Q1.00_0.00_0.00	0.00 ± 0.00	$1.0212\text{e-}03 \pm 1.5578\text{e-}05$
73	2	Q1.00_0.00_0.40	86.52 ± 2.94	$1.1222\text{e-}03 \pm 1.6170\text{e-}05$
74	3	Q1.00_0.00_0.60	121.67 ± 3.10	$1.1867\text{e-}03 \pm 2.2864\text{e-}05$
75	4	Q1.00_0.00_0.80	150.41 ± 3.36	$1.2583\text{e-}03 \pm 2.6838\text{e-}05$
76	5	Q1.00_0.20_0.80	100.21 ± 3.15	$1.3354\text{e-}03 \pm 2.4063\text{e-}05$
77	6	Q1.00_0.40_0.40	187.24 ± 3.13	$1.0215\text{e-}03 \pm 1.2137\text{e-}05$
78	7	Q1.00_0.40_0.80	56.81 ± 2.97	$1.4303\text{e-}03 \pm 4.4059\text{e-}05$
79	8	Q1.00_0.60_0.60	278.63 ± 3.61	$1.0291\text{e-}03 \pm 1.2899\text{e-}05$
80	9	Q1.00_0.80_0.80	370.96 ± 4.17	$1.0364\text{e-}03 \pm 1.3484\text{e-}05$
81	10	Q1.33_0.00_0.25	141.93 ± 7.04	$9.0970\text{e-}04 \pm 2.0439\text{e-}05$
82	11	Q1.33_0.80_0.45	224.08 ± 8.04	$9.8985\text{e-}04 \pm 2.3984\text{e-}05$
83	12	Q1.33_0.80_0.45	324.51 ± 7.06	$9.7709\text{e-}04 \pm 2.1414\text{e-}05$
84	13	Q1.33_0.80_0.60	100.95 ± 7.30	$7.5206\text{e-}04 \pm 1.9400\text{e-}05$
85	14	Q1.33_0.80_0.60	31.53 ± 6.81	$1.4439\text{e-}03 \pm 5.1518\text{e-}05$
86	15	Q1.33_0.80_0.80	429.46 ± 6.98	$8.9441\text{e-}04 \pm 2.0003\text{e-}05$
87	16	Q2.00_0.00_0.50	280.29 ± 10.11	$6.4881\text{e-}04 \pm 1.5696\text{e-}05$
88	17	Q2.00_0.00_0.50	56.14 ± 18.31	$9.8041\text{e-}04 \pm 3.6214\text{e-}05$
89	18	Q2.00_0.80_0.20	106.68 ± 17.67	$7.8122\text{e-}04 \pm 2.0382\text{e-}05$
90	19	Q2.00_0.80_0.20	272.75 ± 10.36	$7.7112\text{e-}04 \pm 1.9656\text{e-}05$
91	20	Q2.00_0.80_0.40	186.81 ± 11.35	$6.3521\text{e-}04 \pm 1.6695\text{e-}05$
92	21	Q2.00_0.80_0.40	90.59 ± 10.69	$1.0226\text{e-}03 \pm 2.9113\text{e-}05$
93	22	Q2.00_0.80_0.80	275.34 ± 9.70	$5.6439\text{e-}04 \pm 1.5505\text{e-}05$
94	23	Q2.00_0.80_0.80	163.32 ± 13.49	$1.0474\text{e-}03 \pm 4.9487\text{e-}05$
95	24	Q2.00_0.80_0.80	427.96 ± 9.46	$6.2197\text{e-}04 \pm 1.5299\text{e-}05$
96	25	Q2.00_0.80_0.80	13.46 ± 13.54	$1.3322\text{e-}03 \pm 7.5317\text{e-}05$
97	26	Q3.00_0.00_0.67	295.28 ± 8.30	$3.9392\text{e-}04 \pm 7.5159\text{e-}06$
98	27	Q3.00_0.00_0.67	41.95 ± 17.23	$7.8909\text{e-}04 \pm 4.8042\text{e-}05$
99	28	Q3.00_0.80_0.80	75.01 ± 7.80	$8.4159\text{e-}04 \pm 3.6205\text{e-}05$
100	29	Q3.00_0.80_0.80	353.28 ± 6.68	$3.8485\text{e-}04 \pm 5.5913\text{e-}06$
101	30	Q4.00_0.00_0.75	255.84 ± 10.72	$2.7338\text{e-}04 \pm 1.0862\text{e-}05$
102	31	Q4.00_0.00_0.75	24.50 ± 14.64	$6.3280\text{e-}04 \pm 5.7880\text{e-}05$
103	32	Q4.00_0.80_0.80	280.92 ± 10.50	$2.7095\text{e-}04 \pm 1.1017\text{e-}05$
104	33	Q5.00_0.00_0.80	212.13 ± 8.03	$1.9439\text{e-}04 \pm 1.0722\text{e-}05$
105	34	Q5.00_0.00_0.80	15.46 ± 10.17	$5.2483\text{e-}04 \pm 4.9141\text{e-}05$
106	35	Q6.00_0.00_0.83	177.69 ± 7.63	$1.4863\text{e-}04 \pm 1.0792\text{e-}05$
107	36	Q6.00_0.00_0.83	11.07 ± 8.55	$4.3456\text{e-}04 \pm 5.4457\text{e-}05$

Appendix B: Convergence studies

For the recoil velocity and peak luminosity calculations, there are two main sources of error. The first is the error from calculating the values at a finite observer location. The second, and typically of comparable magnitude, is from finite resolution. Since the final mass and spin are calculated locally on the apparent horizon, where the grid resolution is highest, the finite resolution error is very low and there is no associated finite observer error, hence those quantities can be determined to high accuracy. In order to get a sense of the error of other radiated quantities, we can calculate the final mass and spin in an analogous way we calculate the recoil and luminosity. In this appendix, we will explore these errors and the convergence of a set of simulations.

For every simulation, we can calculate the finite observer location error. However, in order to calculate the finite resolution error, we would need the same binary configuration at three different resolutions. For 107 runs, this would be very expensive computationally. Instead, we choose a simulation from each mass ratio at three different resolutions and use this run to calculate the finite resolution error. This error is then used as a weight in the least-squares fitting for the corresponding family of the same mass ratio runs.

The kicks and luminosity values included in the tables are calculated using up to $\ell = 6$ modes at an extraction radius of $r_{obs}/M = 113.0$. To extrapolate to infinite observer location, we use the perturbative extrapolation given in Ref. [36]. There is typically still some residual r -dependence so to calculate the extrapolation error we take the difference between the value calculated at $r_{obs} = 113.0M$ and extrapolating to $r_{obs} = \infty$ using the average of a first and second order polynomial in $1/r_{obs}$. This is typically on the order of 1 – 3 km/s but for a few runs is higher.

We can estimate the finite resolution error by using three different resolutions and a Richardson extrapolation. We label our resolutions as NX where X is a global resolution factor that is related to the resolution in the wavezone. For example, a simulation labeled $N140$ would have a wavezone resolution of $M/1.4$. Tables XIV-XVII show the values of the kick and luminosity at each extraction radius and extrapolated to infinite resolution, along with the order of convergence for each. We typically observe a convergence order between 2.5 and 4 with

slightly lower convergence order for the $q = 1/3$ luminosity. The fitting weights are determined from these tables as the difference between the $(r_{obs}, N) = (\infty, \infty)$ and $(113.0M, \text{finite})$, where N is the resolution factor as described above. This leads to finite resolution errors typically on the order of 5 – 15 km/s for the recoil. The total error reported in Tables XI-XIII is the finite observer and finite resolution errors added in quadrature.

In Figs. 8-11, we show the recoil velocity, peak luminosity, radiated energy, and radiated angular momentum for each resolution as a function of the inverse of the

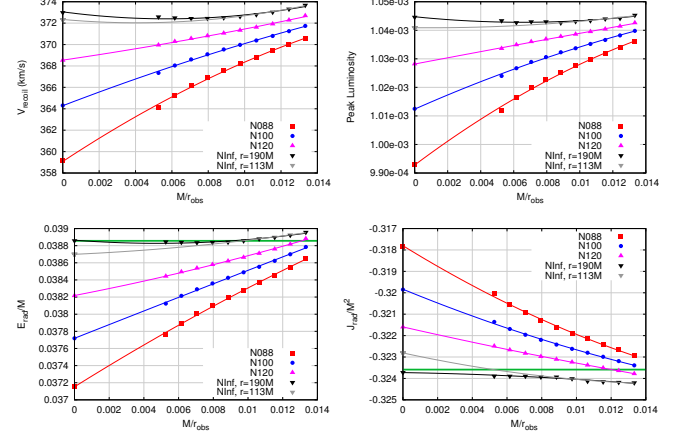


FIG. 8. Plots of the convergence of the recoil velocity (top left), peak luminosity (top right), energy radiated (bottom left), and angular momentum radiated (bottom right) as a function of M/r_{obs} for case 80 - Q1.0000-0.8000-0.8000. Horizontal green solid lines in the bottom row indicate the energy and angular momentum radiated calculated from the isolated horizon. The dark gray lines in each plot shows the extrapolation to infinite observer location using only up to $r = 113M$.

observer location. For the radiated energy and angular momentum, the value calculated on the isolated horizon is shown as a green solid line. In each, the solid lines indicate a second order polynomial fit in M/r_{obs} to extrapolate to infinite observer location. In all cases, we have six extraction radii between $75M$ and $113M$. For the equal-mass case in Fig. 8, we have an additional four extraction radii, out to $190M$. In this figure, we show two extrapolations to infinite observer, one in black using all available extraction radii, and one in gray using only up to $r_{obs} = 113M$ as in the other figures. The difference between the two extrapolations is on the order of 1% for all four quantities.

-
- [1] F. Pretorius, Phys. Rev. Lett. **95**, 121101 (2005), gr-qc/0507014.
 - [2] M. Campanelli, C. O. Lousto, P. Marronetti, and Y. Zlochower, Phys. Rev. Lett. **96**, 111101 (2006), gr-qc/0511048.
 - [3] J. G. Baker, J. Centrella, D.-I. Choi, M. Koppitz, and

- J. van Meter, Phys. Rev. Lett. **96**, 111102 (2006), gr-qc/0511103.
- [4] M. Campanelli, C. O. Lousto, H. Nakano, and Y. Zlochower, Phys. Rev. **D79**, 084010 (2009), arXiv:0808.0713 [gr-qc].
- [5] B. P. Abbott *et al.* (Virgo, LIGO Scientific), Phys. Rev.

TABLE XIV. Convergence of the recoil velocity V and peak luminosity L for each observer location r_{obs}/M for case 80 - Q1.0000-0.8000.0.8000. Subscripts on the recoil and luminosity indicate low, medium, high, and extrapolated to infinite spatial resolution. For this case, the three resolutions are N088, N100, and N120. The order of convergence is given for both the recoil, d_V , and the luminosity d_L .

r_{obs}/M	V_{low}	V_{med}	V_{high}	V_{∞}	d_V	L_{low}	L_{med}	L_{high}	L_{∞}	d_L
75.00	370.59	371.74	372.69	373.68	3.66	1.0362e-03	1.0398e-03	1.0426e-03	1.0453e-03	3.97
80.41	369.98	371.25	372.28	373.32	3.76	1.0340e-03	1.0382e-03	1.0414e-03	1.0442e-03	4.18
86.66	369.40	370.80	371.92	373.03	3.83	1.0319e-03	1.0366e-03	1.0404e-03	1.0440e-03	3.88
93.96	368.81	370.38	371.61	372.80	3.90	1.0297e-03	1.0352e-03	1.0395e-03	1.0434e-03	4.00
102.60	368.22	369.97	371.33	372.63	3.94	1.0276e-03	1.0337e-03	1.0386e-03	1.0431e-03	3.94
113.00	367.59	369.54	371.06	372.51	3.95	1.0252e-03	1.0323e-03	1.0378e-03	1.0426e-03	4.13
125.74	366.91	369.09	370.81	372.45	3.92	1.0228e-03	1.0306e-03	1.0369e-03	1.0430e-03	3.84
141.71	366.13	368.61	370.56	372.44	3.89	1.0198e-03	1.0289e-03	1.0360e-03	1.0430e-03	3.85
162.34	365.23	368.04	370.28	372.50	3.82	1.0163e-03	1.0267e-03	1.0349e-03	1.0427e-03	3.93
190.00	364.11	367.35	369.95	372.59	3.76	1.0120e-03	1.0240e-03	1.0336e-03	1.0434e-03	3.75
∞	359.14	364.31	368.53	372.99	3.65	9.9307e-04	1.0125e-03	1.0282e-03	1.0446e-03	3.69

TABLE XV. Convergence of the recoil velocity V and peak luminosity L for each observer location r_{obs}/M for case 47 - Q0.7500-0.8000.0.8000. Subscripts on the recoil and luminosity indicate low, medium, high, and extrapolated to infinite spatial resolution. For this case, the three resolutions are N100, N120, and N140. The order of convergence is given for both the recoil, d_V , and the luminosity d_L .

r_{obs}/M	V_{low}	V_{med}	V_{high}	V_{∞}	d_V	L_{low}	L_{med}	L_{high}	L_{∞}	d_L
75.00	286.34	288.87	290.04	291.65	3.55	1.1190e-03	1.1278e-03	1.1318e-03	1.1371e-03	3.63
80.41	285.84	288.51	289.74	291.42	3.57	1.1168e-03	1.1260e-03	1.1303e-03	1.1363e-03	3.50
86.66	285.34	288.18	289.48	291.22	3.61	1.1144e-03	1.1244e-03	1.1289e-03	1.1352e-03	3.57
93.96	284.85	287.86	289.23	291.06	3.64	1.1120e-03	1.1229e-03	1.1278e-03	1.1341e-03	3.73
102.60	284.33	287.55	289.01	290.95	3.65	1.1100e-03	1.1215e-03	1.1267e-03	1.1336e-03	3.65
113.00	283.76	287.23	288.80	290.85	3.69	1.1075e-03	1.1200e-03	1.1256e-03	1.1327e-03	3.78
∞	278.24	284.47	287.20	290.56	3.86	1.0853e-03	1.1083e-03	1.1175e-03	1.1271e-03	4.39

TABLE XVI. Convergence of the recoil velocity V and peak luminosity L for each observer location r_{obs}/M for case 67 - Q0.5000-0.0000.0.0000. Subscripts on the recoil and luminosity indicate low, medium, high, and extrapolated to infinite spatial resolution. For this case, the three resolutions are N100, N120, and N140. The order of convergence is given for both the recoil, d_V , and the luminosity d_L .

r_{obs}/M	V_{low}	V_{med}	V_{high}	V_{∞}	d_V	L_{low}	L_{med}	L_{high}	L_{∞}	d_L
75.00	150.53	153.11	154.44	156.81	2.90	7.7159e-04	7.7751e-04	7.7976e-04	7.8189e-04	4.68
80.41	149.84	152.59	154.02	156.53	2.91	7.6977e-04	7.7593e-04	7.7829e-04	7.8056e-04	4.63
86.66	149.14	152.09	153.63	156.42	2.84	7.6785e-04	7.7448e-04	7.7698e-04	7.7929e-04	4.75
93.96	148.46	151.61	153.26	156.31	2.81	7.6622e-04	7.7315e-04	7.7579e-04	7.7828e-04	4.69
102.60	147.75	151.13	152.91	156.20	2.80	7.6446e-04	7.7186e-04	7.7478e-04	7.7772e-04	4.48
113.00	147.00	150.63	152.56	156.24	2.74	7.6283e-04	7.7075e-04	7.7383e-04	7.7684e-04	4.57
∞	139.67	146.00	149.53	157.20	2.45	7.4753e-04	7.6123e-04	7.6708e-04	7.7389e-04	4.02

TABLE XVII. Convergence of the recoil velocity V and peak luminosity L for each observer location r_{obs}/M for case 65 - Q0.3333-0.0000.0.0000. Subscripts on the recoil and luminosity indicate low, medium, high, and extrapolated to infinite spatial resolution. For this case, the three resolutions are N100, N120, and N140. The order of convergence is given for both the recoil, d_V , and the luminosity d_L .

r_{obs}/M	V_{low}	V_{med}	V_{high}	V_{∞}	d_V	L_{low}	L_{med}	L_{high}	L_{∞}	d_L
75.00	172.27	175.62	177.39	180.65	2.80	5.2641e-04	5.2929e-04	5.3117e-04	5.3812e-04	1.55
80.41	171.36	174.96	176.85	180.34	2.81	5.2503e-04	5.2812e-04	5.3012e-04	5.3741e-04	1.58
86.66	170.45	174.30	176.34	180.18	2.76	5.2355e-04	5.2702e-04	5.2916e-04	5.3563e-04	1.86
93.96	169.52	173.64	175.84	180.06	2.72	5.2229e-04	5.2601e-04	5.2827e-04	5.3467e-04	1.96
102.60	168.57	172.98	175.36	180.00	2.68	5.2082e-04	5.2509e-04	5.2749e-04	5.3289e-04	2.39
113.00	167.58	172.32	174.88	179.99	2.64	5.1950e-04	5.2413e-04	5.2672e-04	5.3241e-04	2.43
∞	157.63	165.82	170.51	181.52	2.30	5.0628e-04	5.1631e-04	5.2069e-04	5.2603e-04	3.89

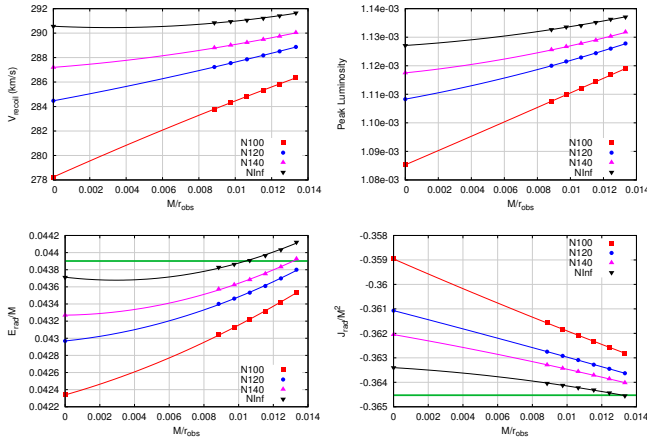


FIG. 9. Plots of the convergence of the recoil velocity (top left), peak luminosity (top right), energy radiated (bottom left), and angular momentum radiated (bottom right) as a function of M/r_{obs} for case 47 - Q0.7500-0.8000-0.8000. Horizontal green solid lines in the bottom row indicate the energy and angular momentum radiated calculated from the isolated horizon.

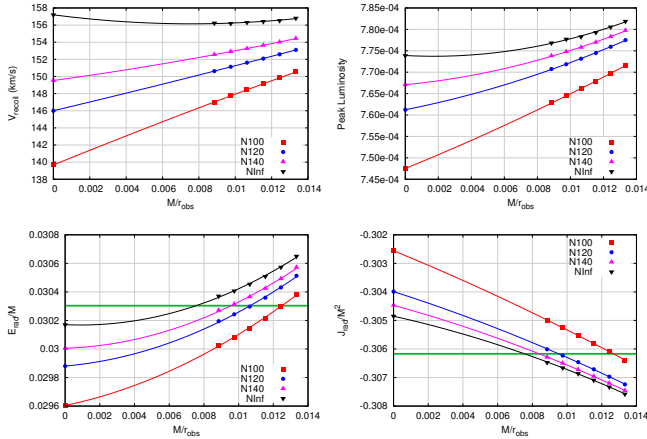


FIG. 10. Plots of the convergence of the recoil velocity (top left), peak luminosity (top right), energy radiated (bottom left), and angular momentum radiated (bottom right) as a function of M/r_{obs} for case 67 - Q0.5000-0.0000-0.0000. Horizontal green solid lines in the bottom row indicate the energy and angular momentum radiated calculated from the isolated horizon.

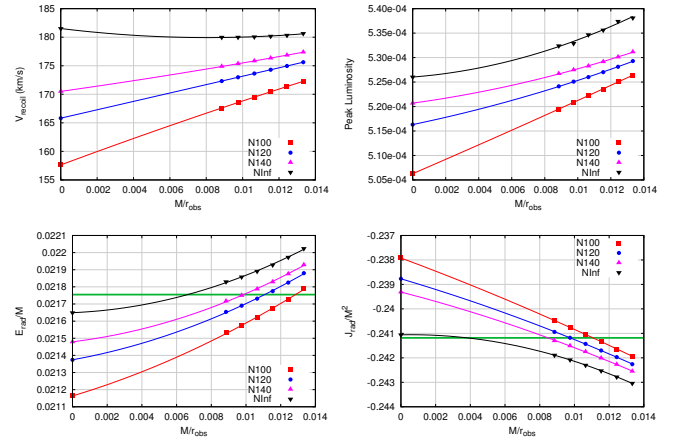


FIG. 11. Plots of the convergence of the recoil velocity (top left), peak luminosity (top right), energy radiated (bottom left), and angular momentum radiated (bottom right) as a function of M/r_{obs} for case 65 - Q0.3333-0.0000-0.0000. Horizontal green solid lines in the bottom row indicate the energy and angular momentum radiated calculated from the isolated horizon.

- Lett. **116**, 241102 (2016), arXiv:1602.03840 [gr-qc].
- [6] B. Abbott *et al.* (Virgo, LIGO Scientific), Phys. Rev. Lett. **116**, 061102 (2016), arXiv:1602.03837 [gr-qc].
- [7] B. P. Abbott *et al.* (Virgo, LIGO Scientific), Phys. Rev. Lett. **116**, 241103 (2016), arXiv:1606.04855 [gr-qc].
- [8] B. P. Abbott *et al.* (Virgo, LIGO Scientific), (2016), arXiv:1606.04856 [gr-qc].
- [9] G. Lovelace *et al.*, (2016), arXiv:1607.05377 [gr-qc].
- [10] M. Campanelli, C. O. Lousto, and Y. Zlochower, Phys. Rev. **D74**, 041501(R) (2006), gr-qc/0604012.
- [11] M. Campanelli, C. O. Lousto, Y. Zlochower, and D. Merritt, Astrophys. J. **659**, L5 (2007), gr-qc/0701164.

- [12] M. Campanelli, C. O. Lousto, Y. Zlochower, and D. Merritt, Phys. Rev. Lett. **98**, 231102 (2007), gr-qc/0702133.
- [13] C. O. Lousto and Y. Zlochower, Phys. Rev. Lett. **107**, 231102 (2011), arXiv:1108.2009 [gr-qc].
- [14] C. O. Lousto and J. Healy, Phys. Rev. Lett. **114**, 141101 (2015), arXiv:1410.3830 [gr-qc].
- [15] C. O. Lousto, J. Healy, and H. Nakano, Phys. Rev. **D93**, 044031 (2016), arXiv:1506.04768 [gr-qc].
- [16] C. O. Lousto and J. Healy, (2016), arXiv:1601.05086 [gr-qc].
- [17] J. Healy, C. O. Lousto, and Y. Zlochower, Phys. Rev. **D90**, 104004 (2014), arXiv:1406.7295 [gr-qc].
- [18] A. H. Mroue, M. A. Scheel, B. Szilagyi, H. P. Pfeiffer, M. Boyle, *et al.*, Phys. Rev. Lett. **111**, 241104 (2013), arXiv:1304.6077 [gr-qc].
- [19] K. Jani, J. Healy, J. A. Clark, L. London, P. Laguna, and D. Shoemaker, (2016), arXiv:1605.03204 [gr-qc].
- [20] B. P. Abbott *et al.* (Virgo, LIGO Scientific), (2016), arXiv:1606.01262 [gr-qc].
- [21] Y. Zlochower, J. G. Baker, M. Campanelli, and C. O. Lousto, Phys. Rev. **D72**, 024021 (2005), arXiv:gr-qc/0505055.
- [22] P. Marronetti, W. Tichy, B. Brüggmann, J. Gonzalez, and U. Sperhake, Phys. Rev. **D77**, 064010 (2008), arXiv:0709.2160 [gr-qc].
- [23] C. O. Lousto and Y. Zlochower, Phys. Rev. **D77**, 024034 (2008), arXiv:0711.1165 [gr-qc].
- [24] Y. Zlochower, M. Ponce, and C. O. Lousto, Phys. Rev. **D86**, 104056 (2012), arXiv:1208.5494 [gr-qc].
- [25] <https://portal.xsede.org/sdsc-comet>.
- [26] C. O. Lousto and Y. Zlochower, Phys. Rev. **D88**, 024001 (2013), arXiv:1304.3937 [gr-qc].
- [27] F. Löffler, J. Faber, E. Bentivegna, T. Bode, P. Diener, R. Haas, I. Hinder, B. C. Mundim, C. D. Ott, E. Schnetter, G. Allen, M. Campanelli, and P. Laguna, Class. Quant. Grav. **29**, 115001 (2012), arXiv:1111.3344 [gr-qc].
- [28] Einstein Toolkit home page: <http://einstein toolkit.org>.

- [29] Cactus Computational Toolkit home page: <http://cactuscode.org>.
- [30] E. Schnetter, S. H. Hawley, and I. Hawke, *Class. Quant. Grav.* **21**, 1465 (2004), gr-qc/0310042.
- [31] J. Thornburg, *Class. Quant. Grav.* **21**, 743 (2004), gr-qc/0306056.
- [32] O. Dreyer, B. Krishnan, D. Shoemaker, and E. Schnetter, *Phys. Rev.* **D67**, 024018 (2003), gr-qc/0206008.
- [33] M. Campanelli, C. O. Lousto, Y. Zlochower, B. Krishnan, and D. Merritt, *Phys. Rev.* **D75**, 064030 (2007), gr-qc/0612076.
- [34] M. Campanelli and C. O. Lousto, *Phys. Rev.* **D59**, 124022 (1999), arXiv:gr-qc/9811019 [gr-qc].
- [35] C. O. Lousto and Y. Zlochower, *Phys. Rev.* **D76**, 041502(R) (2007), gr-qc/0703061.
- [36] H. Nakano, J. Healy, C. O. Lousto, and Y. Zlochower, *Phys. Rev.* **D91**, 104022 (2015), arXiv:1503.00718 [gr-qc].
- [37] J. G. Baker, M. Campanelli, C. O. Lousto, and R. Takahashi, *Phys. Rev.* **D69**, 027505 (2004), arXiv:astro-ph/0305287.
- [38] E. Barausse, V. Morozova, and L. Rezzolla, *Astrophys. J.* **758**, 63 (2012), arXiv:1206.3803 [gr-qc].
- [39] L. Rezzolla, E. Barausse, E. N. Dorband, D. Pollney, C. Reisswig, J. Seiler, and S. Husa, *Phys. Rev.* **D78**, 044002 (2008), arXiv:0712.3541 [gr-qc].
- [40] F. Hofmann, E. Barausse, and L. Rezzolla, *Astrophys. J.* **825**, L19 (2016), arXiv:1605.01938 [gr-qc].
- [41] C. O. Lousto, M. Campanelli, Y. Zlochower, and H. Nakano, *Class. Quant. Grav.* **27**, 114006 (2010), arXiv:0904.3541 [gr-qc].
- [42] C. O. Lousto and Y. Zlochower, *Phys. Rev.* **D89**, 104052 (2014), arXiv:1312.5775 [gr-qc].
- [43] Y. Zlochower and C. O. Lousto, *Phys. Rev.* **D92**, 024022 (2015), arXiv:1503.07536 [gr-qc].
- [44] M. Campanelli, C. O. Lousto, and Y. Zlochower, *Phys. Rev.* **D79**, 084012 (2009), arXiv:0811.3006 [gr-qc].
- [45] R. Owen, *Phys. Rev.* **D81**, 124042 (2010), arXiv:1004.3768 [gr-qc].
- [46] <https://dcc.ligo.org/public/0123/T1600018/004/PeakLuminosityUIB-public.pdf>.
- [47] C. O. Lousto and Y. Zlochower, *Phys. Rev.* **D87**, 084027 (2013), arXiv:1211.7099 [gr-qc].
- [48] J. G. Baker, M. Campanelli, and C. O. Lousto, *Phys. Rev.* **D65**, 044001 (2002), arXiv:gr-qc/0104063 [gr-qc].
- [49] S. Husa, M. Hannam, J. A. Gonzalez, U. Sperhake, and B. Brügmann, *Phys. Rev.* **D77**, 044037 (2008), arXiv:0706.0904 [gr-qc].
- [50] H. P. Pfeiffer, D. A. Brown, L. E. Kidder, L. Lindblom, G. Lovelace, and M. A. Scheel, *New frontiers in numerical relativity. Proceedings, International Meeting, NFN 2006, Potsdam, Germany, July 17-21, 2006*, *Class. Quant. Grav.* **24**, S59 (2007), arXiv:gr-qc/0702106 [gr-qc].
- [51] S. Brandt and B. Brügmann, *Phys. Rev. Lett.* **78**, 3606 (1997), gr-qc/9703066.
- [52] <http://www.black-holes.org/waveforms>.
- [53] R. Fujita, *PTEP* **2015**, 033E01 (2015), arXiv:1412.5689 [gr-qc].
- [54] J. A. González, M. D. Hannam, U. Sperhake, B. Brügmann, and S. Husa, *Phys. Rev. Lett.* **98**, 231101 (2007), gr-qc/0702052.
- [55] B. Krishnan, C. O. Lousto, and Y. Zlochower, *Phys. Rev.* **D76**, 081501 (2007), arXiv:0707.0876 [gr-qc].
- [56] B. P. Abbott *et al.* (Virgo, LIGO Scientific), *Phys. Rev. Lett.* **116**, 221101 (2016), arXiv:1602.03841 [gr-qc].